Imaging crossing fibers in mouse, pig, monkey, and human brain using small-angle X-ray scattering

Georgiadis, Marios; Menzel, Miriam; Reuter, Jan A.; Born, Donald E.; Kovacevich, Sophie R.; Alvarez, Dario; Taghavi, Hossein Moein; Schroeter, Aileen; Rudin, Markus; More Authors

DOI
10.1016/j.actbio.2023.04.029

Publication date
2023

Document Version
Final published version

Published in
Acta Biomaterialia

Citation (APA)
Georgiadis, M., Menzel, M., Reuter, J. A., Born, D. E., Kovacevich, S. R., Alvarez, D., Taghavi, H. M., Schroeter, A., Rudin, M., & More Authors (2023). Imaging crossing fibers in mouse, pig, monkey, and human brain using small-angle X-ray scattering. *Acta Biomaterialia*, *164*, 317-331. https://doi.org/10.1016/j.actbio.2023.04.029

Acta Biomaterialia 164 (2023) 317–331

Contents lists available at ScienceDirect

Acta Biomaterialia

journal homepage: www.elsevier.com/locate/actbio

Full length article

Imaging crossing fibers in mouse, pig, monkey, and human brain using small-angle X-ray scattering

Marios Georgiadis[a,b,*], Miriam Menzel[c,d], Jan A Reuter[c], Donald E Born[e], Sophie R Kovacevich[a], Dario Alvarez[a], Hossein Moein Taghavi[a], Aileen Schroeter[b], Markus Rudin[b], Zirui Gao[b], Manuel Guizar-Sicairos[f], Thomas M Weiss[g], Markus Axer[c], Ivan Rajkovic[g], Michael M Zeineh[a]

[a] Department of Radiology, Stanford School of Medicine, Stanford, CA, USA
[b] Institute for Biomedical Engineering, ETH Zurich and University of Zurich, Zurich, Switzerland
[c] Institute of Neuroscience and Medicine (INM-1), Forschungszentrum Jülich GmbH, Jülich 52425, Germany
[d] Department of Imaging Physics, Delft University of Technology, Delft, the Netherlands
[e] Department of Pathology, Stanford School of Medicine, Stanford, CA, USA
[f] Photon Science Division, Paul Scherrer Institute, Villigen, Switzerland
[g] SLAC National Accelerator Laboratory, Stanford Synchrotron Radiation Lightsource, USA

ARTICLE INFO

Article history:
Received 28 November 2022
Revised 15 April 2023
Accepted 18 April 2023
Available online 23 April 2023

Keywords:
Crossing fibers
Scanning small-angle X-ray scattering (SAXS)
Animal and human brain
Mouse/pig/vervet monkey brain
Human hippocampus
Imaging myelinated axons
Fiber orientation mapping
Diffusion MRI

ABSTRACT

Myelinated axons (nerve fibers) efficiently transmit signals throughout the brain via action potentials. Multiple methods that are sensitive to axon orientations, from microscopy to magnetic resonance imaging, aim to reconstruct the brain's structural connectome. As billions of nerve fibers traverse the brain with various possible geometries at each point, resolving fiber crossings is necessary to generate accurate structural connectivity maps. However, doing so with specificity is a challenging task because signals originating from oriented fibers can be influenced by brain (micro)structures unrelated to myelinated axons.

X-ray scattering can specifically probe myelinated axons due to the periodicity of the myelin sheath, which yields distinct peaks in the scattering pattern. Here, we show that small-angle X-ray scattering (SAXS) can be used to detect myelinated, axon-specific fiber crossings. We first demonstrate the capability using strips of human corpus callosum to create artificial double- and triple-crossing fiber geometries, and we then apply the method in mouse, pig, vervet monkey, and human brains. We compare results to polarized light imaging (3D-PLI), tracer experiments, and to outputs from diffusion MRI that sometimes fails to detect crossings. Given its specificity, capability of 3-dimensional sampling and high resolution, SAXS could serve as a ground truth for validating fiber orientations derived using diffusion MRI as well as microscopy-based methods.

Statement of significance

To study how the nerve fibers in our brain are interconnected, scientists need to visualize their trajectories, which often cross one another. Here, we show the unique capacity of small-angle X-ray scattering (SAXS) to study these fiber crossings without use of labeling, taking advantage of SAXS's specificity to myelin - the insulating sheath that is wrapped around nerve fibers. We use SAXS to detect double and triple crossing fibers and unveil intricate crossings in mouse, pig, vervet monkey, and human brains. This non-destructive method can uncover complex fiber trajectories and validate other less specific imaging methods (e.g., MRI or microscopy), towards accurate mapping of neuronal connectivity in the animal and human brain.

Abbreviations: SAXS, small-angle X-ray scattering.

* Corresponding author at: Department of Radiology, Stanford School of Medicine, Stanford, CA, USA.
E-mail address: mariosg@stanford.edu (M. Georgiadis).

https://doi.org/10.1016/j.actbio.2023.04.029
1742-7061/

1. Introduction

Signals in the brain are transmitted within neurons via action potentials. These are typically initiated in the soma of neurons, and travel through neuronal axons (nerve fibers) until they reach the synaptic clefts where biochemical mechanisms further transmit the signals to the next cell. A major evolutionary step in the signal transmission in the brain came with myelination: oligodendrocytes, an abundant type of central nervous system glial cells found in vertebrates, form processes that "wrap around" neuronal axons (Schwann cells do the same in the peripheral nervous system). The resulting layered structure around axons is called myelin (with a layer periodicity of ∼15-20 nm) and is an essential component of our brain, constituting ∼35% of its dry weight [1].

In the beginning of the 21st century, the term "brain connectome" was coined [2,3], with the goal of mapping neuronal connections across the animal and human brain. Given that there are >50 billion neurons in a human brain [4], with more than 100,000 km total length of myelinated fibers [5], each of diameter from 0.1 to 100 µm [6] (with most axons being around 1 µm in diameter), mapping all their connections is an immensely difficult task, for which we currently lack adequate imaging solutions. However, multiple technologies have been and are being developed to tackle this problem.

Neuronal tracers are considered the gold standard for animal neuronal connectivity, as they are confined to the intracellular compartment and allow tracing a number of neuronal paths throughout the animal brain [7,8], with the mouse brain having been studied and mapped extensively [7,9,10]. However, the limited ability to study human brains, in addition to the experimental effort for the multiple injections, animals, and imaging sessions needed to cover a subset of the neurons of a typical animal brain makes this unique method inconvenient for standard assessment of structural connectivity.

At the nanometer level, electron microscopy can image at very high resolutions, providing us with exquisite images of post-mortem human and animal brain at the sub-cellular level, where even single myelin layers can be clearly distinguished [11]. However, electron microscopy typically needs extended sample preparation procedures, which can alter the sample microstructure. Also, even when used in 3D, electron microcopy typically images a small part of the brain at these very high resolutions, usually covering a volume of much less than $1 mm^3$.

Alternatively, fluorescence microscopy methods can reach sub-micrometer resolutions and visualize fibers in extended brain regions [12], while tissue clearing can help image large specimens such as whole mouse or rat brains [13]. However, tissue clearing usually involves tissue distortion and is more difficult for larger and non-perfusion-fixed human tissues. Furthermore, the use of structure tensor analysis, typically accompanying these direct microscopy methods for deriving orientation information, is prone to artifacts due to structures other than axons and its application may be difficult in dense white matter regions where intensity gradients are small.

Imaging methods that directly probe axon orientations overcome many of these issues. 3D Polarized Light Imaging (3D-PLI) exploits the birefringence of myelin to derive fiber orientations in tissue sections at micrometer resolution, with the possible field of view extending to the entire human brain [14]. However, it cannot recover crossing fibers within a pixel, though in-plane pixels are sometimes small enough to still resolve individual bundles crossing one another over several pixels (Zeineh et al. [15], Fig 4). Furthermore, the determination of the out-of-plane angle by 3D-PLI is challenging. Polarization-sensitive optical coherence tomography (PS-OCT) in serial, back-scattered mode also provides high-resolution orientation information based on the birefringence of myelin [16,17] while facilitating image registration, but the method has otherwise similar limitations to 3D-PLI. Scattered light imaging (SLI) [18] partly overcomes those challenges, being able to resolve fiber crossings with micrometer resolution, while also providing information on out-of-plane fiber angles. Nonetheless, SLI is a new method that still needs validation, especially regarding the quantification of the out-of-plane fiber angles.

Finally, the most commonly used method to provide brain-wide structural connectivity is diffusion magnetic resonance imaging (dMRI) [19,20]. dMRI is sensitive to the anisotropic movement of water molecules, which is used as a proxy for local tissue orientation. However, resolution is typically limited to the hundred micrometers range *ex vivo*, while its signal is also sensitive to tissue compartments and microstructures other than myelinated axons, such as non-neuronal cells, extracellular matrix, intracellular components, etc. Most methods used for neuronal orientation analysis to validate dMRI are reviewed in Yendiki et al. [21].

X-ray scattering probes tissue microstructure by investigating tissue's interactions with X-ray photons traversing the sample: photons elastically deviating from the main path are recorded by an area detector a few meters downstream. When photons probe a highly repetitive structure such as myelin, they constructively interfere at specific angles, forming Bragg peaks (hereafter referred to as "myelin peaks"). This constructive interference happens at the plane formed between the photon beam and the direction of periodicity of the repeated structure. In the case of myelin layers, this plane is perpendicular to the nerve fiber orientation. This allows the use of the location of the peaks on the detector for determining the orientation of the myelinated axons (cf. Fig. 1 and Georgiadis et al. [22]). Use of neutrons instead of photons yields a plethora of structural and dynamic data [23], which can be used to validate diffusion MRI water dynamics in brain tissue [24]. Mapping fiber orientations is also feasible, yet with lower resolution and specificity than X-ray scattering [25].

While determining 3D fiber orientation from scanning small-angle X-ray scattering (SAXS) signal has been shown in both thin sections using 3D scanning SAXS [22,26,27] and intact tissue specimens using SAXS tensor tomography [28–30], the usage of scanning SAXS to disentangle crossing fibers in the animal and human brain has not yet been shown. Given the high importance of uncovering interwoven fiber trajectories in connectomics, we sought to determine whether SAXS can delineate crossing fibers. We first demonstrate the use of scanning SAXS to image in-plane crossing fibers in artificial crossings created using strips of human corpus callosum stacked on one another at different angles. In these configurations, we show that SAXS can detect crossing fibers at angles down to 25° and distinguish at least 3 crossing fibers. We also demonstrate the detection of crossing fibers in the white and gray matter of brains of multiple species that are actively investigated in connectomics, including mouse, pig, vervet monkey and humans. We compare the SAXS data on crossing fibers in mouse brain and human hippocampus with results from 3D-PLI, tracer experiments, and diffusion MRI. Taken together, we show the potential of scanning SAXS as an imaging tool that is both specific to axonal orientations and sensitive to crossing fiber detection. Scanning SAXS can help uncover complex fiber geometries in challenging regions of animal and human brains and may therefore serve as validation for state-of-the-art fiber orientation methods such as dMRI or SLI.

2. Methods

2.1. Brain samples

For creating a sample with artificial crossings of fiber bundles, several sections from a human corpus callosum were used. The

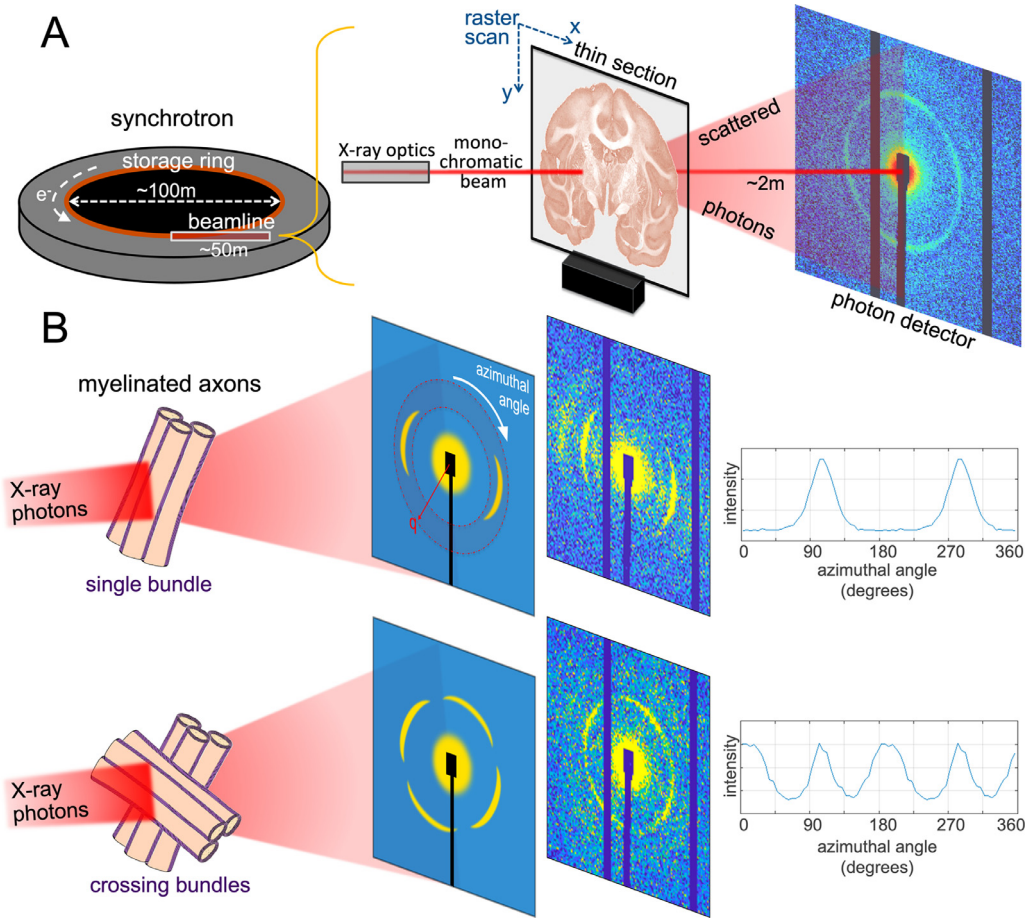

Fig. 1. Detecting myelinated axon orientations using X-ray scattering. (A) Schematic of experimental setup in the synchrotron beamline. The monochromatic X-ray beam impinges the thin section and photons are scattered at small angles according to their interactions with the sample's nanostructure and captured by an area detector. (B) Principle of detecting (crossing) orientations: schematics (left side) and real data (right side) for single (upper panel) and crossing fibers (lower panel). The X-ray photons interact with the periodic myelin layers (left) and produce peaks in the resulting scattering pattern (middle). The radial position (distance from the pattern center, q) of the peak depends on the myelin layer periodicity d ($q = 2\pi/d$), while the azimuthal position depends on the axonal orientations (with photons being scattered at a plane perpendicular to the axon orientation, cf. Georgiadis et al. [22]). To extract exact axonal orientation, the azimuthal profile of the myelin signal across a ring (circumscribed by red dotted lines in the upper scattering pattern sketch) is plotted on the right. The peaks are subsequently identified using the SLIX software (Reuter and Menzel [32]). The position of the peaks in the x-axis (which are always 180° apart due to the center-symmetry of the pattern) reflects the fiber orientation angle. In the scattering patterns, the center area (where the direct, non-scattered beam lands on the detector) is covered by a beamstop that usually includes a photodiode. In addition, the real scattering patterns (middle right panels) have dark stripes (here in the up-down direction) corresponding to detector gaps that accommodate detector electronics. Moreover, the real scattering patterns include multiple orders of the myelin peak, with higher orders at lower intensities, as expected by Bragg's law combined with the form factor of the myelin layer.

brain of a 66-y-o female donor with no sign of neurologic disease was obtained from the Stanford Alzheimer's Disease Research Center Biobank (IRB-approved protocol #33727, including a written informed brain donation consent). It was cut in 1cm coronal slabs, immersion-fixed in 4% paraformaldehyde (PFA) for ~2 weeks, and subsequently stored in a solution of 1x PBS + 0.02% sodium azide to deter bacteria growth. The body of the corpus callosum was excised using a scalpel, and 60 µm sections were cut using a vibratome (VT1000S, Leica Micro-systems, Germany). The corpus callosum from several consecutive sections was manually cut into small, parallel strips of a few millimeters in width. The tissue strips were manually stacked, aiming to create geometries of two or three fibers crossing, similar to the validation sample used for SLI [31]. For scanning, the stacked white matter strips were hydrated by phosphate-buffered saline (PBS) and placed between two 150 µm-thick (#1) cover slips. Cover slips were glued around the edges (Super Glue, The Gorilla Glue Company, USA) to avoid sample dehydration.

The mouse brain sections investigated in this study were previously analyzed [22] to derive single nerve fiber orientations for each tissue pixel. In brief, a vibratome was used to obtain one 25 µm- and one 50 µm-thick coronal section from a 5-month-old C57BL/6 female mouse brain, which had previously been fixed by transcardial perfusion with PBS and 4% PFA and then immersed in 4% PFA at 4 °C for 48 h. Procedures were within the animal license ZH242/14 of the Animal Imaging Center of ETH Zurich/University of Zurich. Sections were stored in PBS at 4 °C. For scanning, they were enclosed in a PBS bath, within two thin Kapton films (Benetec GmbH, Switzerland) and a custom-made metal frame (see Suppl. Fig. 1 in [22]).

The pig brain was extracted from a female 10-week-old micro-Yucatan minipig, following institutional approval. The brain was immersion-fixed in 4% PFA for a month. A coronal slab was cut out of the left hemisphere, and a vibratome (VT1000S, Leica Microsystems, Germany) was used to cut 100 µm sections. The section together with a minute amount of PBS was placed between #1 cover slips, which were then glued around the edges to avoid sample drying.

The vervet monkey brain section was obtained as described in Menzel et al. [31] (IACUC #A11-219). Briefly, the extracted brain

Table 1
Experimental details for SAXS scans.

	2x/3x crossings	mouse	pig	vervet	human
Beamline, Synchrotron*	4-2, SSRL	cSAXS, SLS	4-2, SSRL	4-2, SSRL	4-2, SSRL
Container	#1 coverslips	Kapton tapes	#1 coverslips	#1 coverslips	Kapton tapes
Section thickness (µm)	2×60, 3×60	25 | 50	100	60	75
Beam energy (KeV)	15	12.4 | 16.3	15	17	11
Beam diameter (µm)	125	25 | 50	100	125	100
Motor step size (µm)	125	25 | 50	100	125	100
Field of view (x-y matrix)	38 × 39 | 42 × 46	256 × 400 |080 × 102	140 × 199	309 × 480	136 × 250
Exposure time/frame (ms)	500	050 | 300	500	600	150

* SSRL: Stanford Synchrotron Radiation Lightsource, SLS: Swiss Light Source

was fixed in 4% PFA and embedded in a 20% glycerin and 2% dimethyl sulfoxide solution before freezing. A cryotome (*Polycut CM 3500*, Leica Microsystems, Germany) was used to obtain 60 µm-thick sections, stored in 20% glycerin. For the scanning SAXS experiments, one section (#518) was immersed in PBS for a few weeks, and then placed between #1 coverslips similar to the pig section and corpus callosum strips.

Finally, the human hippocampus section was obtained from the Stanford ADRC Biobank, from the brain of a 80-y-o female donor with a pathologic diagnosis of low Alzheimer's disease (AD staging A1B1C2, Amyloid 1, Braak's 1, Cerad 2, also diagnosed with hippocampal sclerosis of aging, with positive TDP-43 staining). After extraction, the brain was fixed with 4% formaldehyde, cut into 1cm coronal slabs, and stored in PBS. The left hippocampus was excised and a 75 µm section was obtained using a vibratome (VT1000S, Leica Microsystems, Germany). For scanning, similar to the mouse sections, the human brain section was immersed in PBS and enclosed within two thin Kapton films, surrounded by a metal frame.

All animal procedures were in accordance with the National Institutes of Health guidelines for the use and care of laboratory animals and in compliance with the ARRIVE guidelines.

2.2. SAXS scanning

Each section was raster-scanned by the X-ray beam (details in Table 1). SAXS data were collected by a Pilatus 1M detector (Dectris AG, Switzerland) ∼2 m downstream from the sample. A Pilatus 2M was used for the mouse data. The beam diameter and motor step sizes were matched (cf Table 1), constituting the effective pixel size for each scan.

2.3. SAXS data analysis

A silver behenate (AgBe) standard with known periodicity (5.84nm) was used to identify the scattering pattern center and calibrate the sample-to-detector distance and inverse space units. Each scattering pattern was then segregated into 72 azimuthal segments (5° steps). The signal intensity modulation along the radial direction was obtained for each segment. Due to the center-symmetry of the pattern, photon counts from pixels in 180° opposite segments were averaged. This also allows filling in missing information from the regions that correspond to detector electronics (dark bands in scattering patterns, cf. Fig. 1).

The myelin-specific signal for each segment was isolated using procedures similar to those described in Georgiadis et al. [30], i.e. by fitting a polynomial to the radial signal intensity curve, and isolating the 2nd order myelin peak (within the red ring in Fig. 1), which is the most prominent peak in myelin scattering patterns [30]. This allowed creating azimuthal profiles for each point, plotted in Fig. 1B, right. These reflect the orientation of the different populations of myelinated fibers within each probed volume (pixel size × section thickness).

The SLIX software [32], available on https://github.com/3d-pli/SLIX, was used to quantify and visualize orientations of crossing nerve fibers, by detecting the peaks and identifying their position. This software has been developed to detect up to three different fiber orientations per pixel for scattered light imaging [18], where photons also scatter off the sample depending on nano/microstructure orientation and generate angle-dependent azimuthal profiles and associated peaks [33], a nearly identical computational problem to that with SAXS data. Feeding the SAXS azimuthal profile data from each tissue pixel to SLIX yielded up to three in-plane fiber orientations per pixel. The SLIX "*–smoothing fourier*" parameters used were 0.4/0.225 (default settings suggested by [32]), while we used 0.1/0.01 for obtaining the main hippocampal fiber orientations (this smoothens the curve only preserving the main peaks). The length of the colored bars in fiber orientation maps is weighted by the average myelin signal in each pixel.

In the orientation encoded colormaps (e.g., in Figs. 2–7A), each pixel is split into 4 quadrants, to accommodate 4 possible SLIX-derived fiber orientation colors. If there is a single orientation, all 4 quadrants have the same color. If there are 2 orientations, diagonal quadrants have the same color. If there are 3 orientations, 3 quadrants have corresponding color, while the 4th quadrant is black.

2.4. 3D-PLI

The determination of fiber orientations using 3D-PLI was done in an unstained section of a different C57BL/6 mouse brain. The mouse brain was immersion-fixed in 4% buffered PFA. After cryoprotection (20% glycerol), the brain was deep frozen at −70 °C. The brain was serially sectioned along the coronal plane at 60 µm thickness using a cryotome (Leica Microsystems, Germany). Sections were mounted on a glass slide, embedded in 20% glycerol, cover-slipped and sealed with nail polish. The protocol was approved by the institutional animal welfare committee at the Research Centre Jülich, in accordance with the European Union (National Institutes of Health) guidelines for the use and care of laboratory animals.

Polarimetric measurements of the section were done using the polarizing microscope LMP-1 (Taorad GmbH, Germany). The LMP-1 provides a field of view of 2.7 × 2.7 mm^2 and a pixel size of 1.3 µm. Whole mouse brain section scans were carried out tile-wise using a movable specimen stage and a rotating polarizing filter. For each tile, a stack of 18 images was acquired at equidistant rotation angles (±10°) within the range of 0° to 170°. The measured intensity profile for an individual pixel across the stack of image tiles describes a sinusoidal curve that depends on the spatial orientation of fibers within this pixel. The physical description of the light intensity profile was derived from the Jones calculus for linear optics and represents the basis for orientation analysis, as detailed in [34].

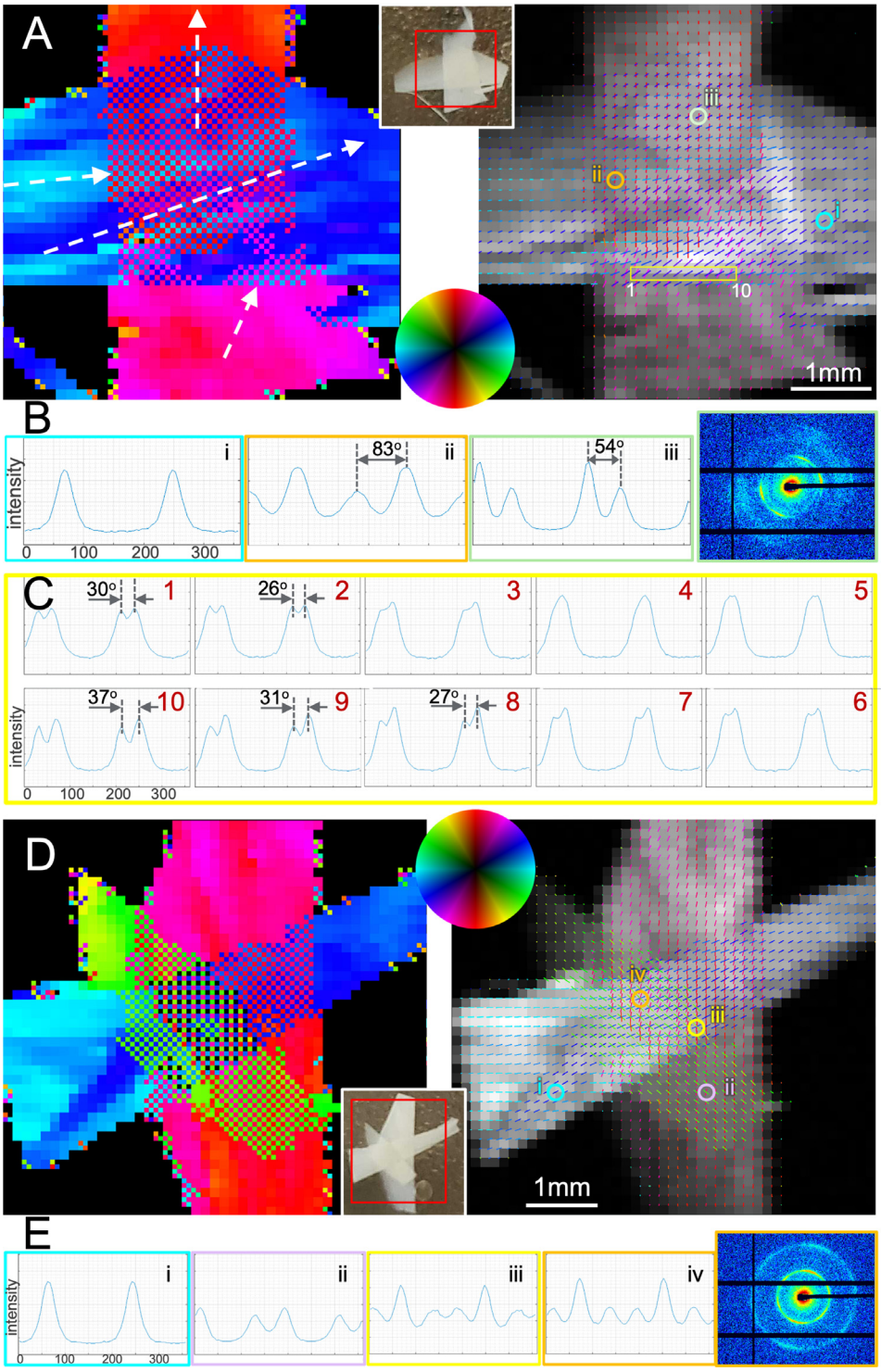

Fig. 2. Scanning SAXS imaging of fiber orientations in a sample containing artificial 2x and 3x crossings prepared using strips of human corpus callosum. (A) Crossing of two fiber bundles. Left panel: fiber orientations for each pixel encoded by the pixel's color, with 4 quadrants per pixel encoding possible multiple orientations as explained in Section 2.3. Right panel: fiber orientations for each pixel are overlaid as colored bars on the azimuthally integrated intensity image, with possible multiple orientations resulting in overlaying bars. Orientation is color-encoded according to the color wheel. Inset: Photo of the fiber strips within the coverslips, with scanned area in red rectangle. (B) Azimuthal intensity profiles (azimuthal scattering intensity across the myelin peak, cf. Fig. 1) for pixels i, ii, and iii, indicated by circles in the right panel of (A). Plot outline colors correspond to the colors of the circles in (A). (C) Azimuthal profiles of 10 subsequent scan points highlighted by yellow rectangle in (A). Profiles show transition from two clearly separate peaks (points 1-2) to one merged peak (points 3-7) and back to two distinct peaks (points 8-10). Data indicate a minimal angle at which SAXS fiber crossings can be identified by the SLIX software of the order of 25-30°. (D) Crossing of three fiber bundles. Left Panel: fiber orientations for each pixel encoded in its color. Right panel: fiber orientations plotted as colored bars. Orientation is encoded by pixel color (left) or bar color (right) according to the color wheel. Inset: Photo of the fiber strips within the coverslips, with scanned area indicated by red rectangle. (E) Azimuthal profiles from select points in (D), with one (cyan), two (magenta), and three (orange & yellow) crossing fibers. As explained in the Methods section, in the colored fiber orientation maps (A), (D) each pixel is split into 4 quadrants, to accommodate 4 possible SLIX-derived fiber orientation colors. For pixels characterized by a single fiber orientation, all 4 quadrants have the same color. For pixels with two crossing fibers, the color of the diagonal quadrants indicates the respective fiber orientations. For pixels with three crossing fibers, 3 quadrants are colorized indicating the respective fiber orientation, while the 4th quadrant is black.

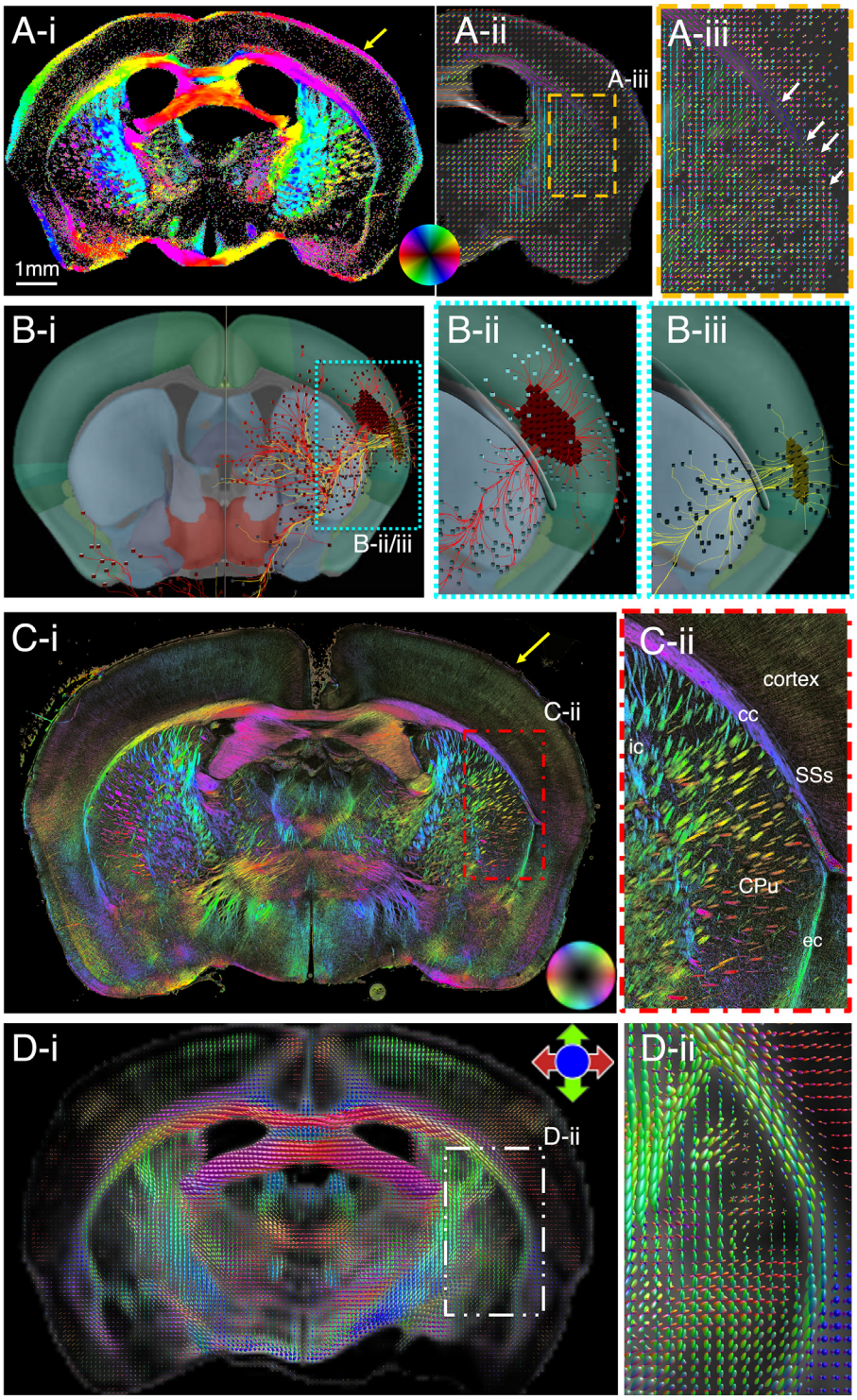

Fig. 3. Fiber orientations in the mouse brain. (A) SAXS-based fiber orientation map of a 25 µm-thick section where the fiber orientation is color-encoded according to the color wheel with 4 quadrants per pixel as described in Section 2.3 (A-i), or with orientation-encoded colored bars (A-ii). To facilitate viewing of the image (A-ii), fiber orientations from each 5×5 pixel set are averaged. (A-iii) Expanded view of orange boxed region in (A-ii), where fibers spreading from the internal capsule through the caudoputamen cross the corpus callosum and external capsule (white arrows) to extend radially into the cortex. In addition, cortical radial fibers reach the outermost molecular layer of the cortex and cross with the circumferential myelinated fibers along the brain surface (yellow arrow in A-i). (B) Visualization of the Allen Mouse Brain Connectivity Atlas experiments 297945448-SSs (B-i) and 520728084-SSs (B-ii) (https://connectivity.brain-map.org/projection/experiment/297945448 and https://connectivity.brain-map.org/projection/experiment/520728084), which included injections in the supplemental somatosensory area, showing axons in red and yellow colors respectively from a C57BL/6J mouse tagged with green fluorescent protein. (B-i) Posterior view of the two experiments. (B-ii/B-iii) Enlarged view of the cyan box in (B-i), with the corpus callosum 3D rendered in semi-transparent gray color to enable visualization of the crossing cortical-caudoputamen fibers. Images generated using the Atlas' 3D viewer (https://connectivity.brain-map.org/3d-viewer). (C) 3D-PLI image showing fiber orientations in a 60 µm-thick mouse brain section, at a plane ~300 µm anterior compared to the section in (A). C-ii is an enlarged view of the red-boxed area in C-i. Yellow arrow points to molecular layer of cortex. (D) Diffusion MRI-derived fiber orientation maps from same mouse and same virtual section as in (A). Fiber orientation distributions are represented by a set of spherical harmonics, allowing multiple fibers per voxel, and are color-encoded according to arrows in top right of (D-i). (D-ii) Enlarged view of white box in D-i, showing no distinguishable corpus callosum crossings. cc: corpus callosum, ic: internal capsule, ec: external capsule, CPu: caudoputamen, SSs: supplemental somatosensory area.

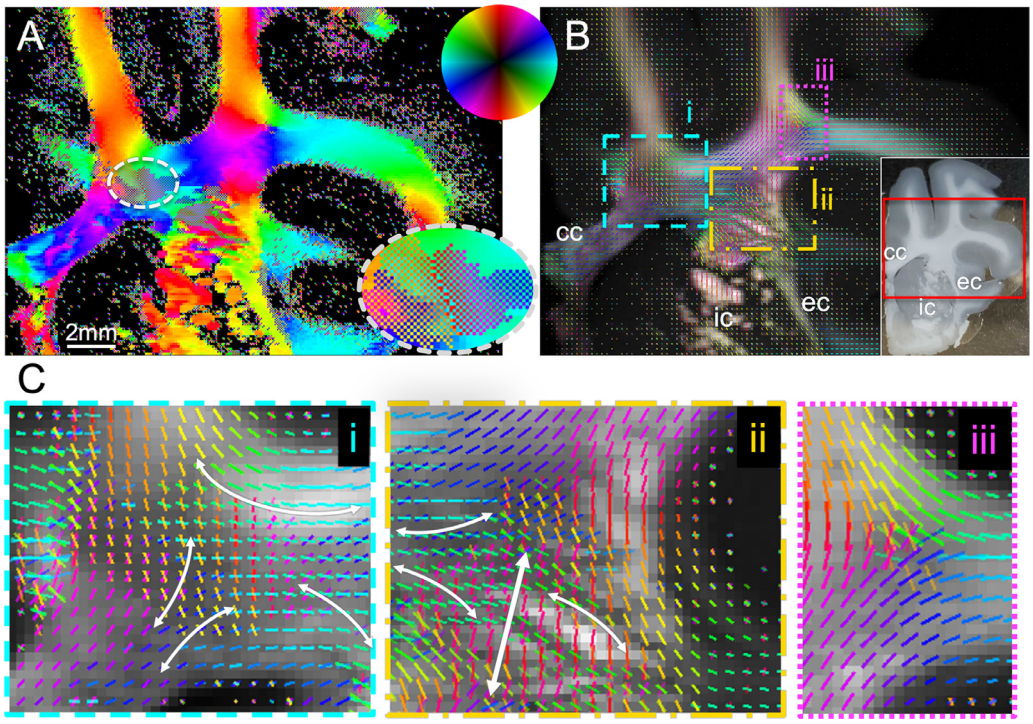

Fig. 4. SAXS-based fiber orientation analysis in a 100 µm-thick coronal brain section of a female 10-week-old micro-Yucatan minipig containing part of the corona radiata. (A) Fiber orientation map with color-encoded fiber orientations according to the color wheel (using 4 quadrants per pixel as described in Section 2.3). Oval inset: enlarged view of the encircled corona radiata region of crossing fibers, with the colors appearing in a checkerboard pattern, due to multiple orientations per pixel displayed in the quadrants. (B) Fiber orientations represented by orientation-encoded colored bars for each 2×2 pixel set. Inset: picture of the pig hemisphere section mounted between the two coverslips, with the red rectangle indicating the region scanned. (C) Subregions of the pig section, enlarged from panel (B), containing areas of two and three fiber crossings, with tracts highlighted with white arrows. cc: corpus callosum, ic: internal capsule, ec: external capsule.

2.5. Diffusion MRI

For diffusion MRI-scanning of the fixed mouse brain, we used a 9.4T Bruker scanner with a volume resonator for transmission and a receive surface cryo-coil. 200 diffusion directions were acquired (20 directions at b-value = 1 ms/µm^2, 40 directions at 2 ms/µm^2, 60 directions at 3 ms/µm^2, 80 directions at 4 ms/µm^2) and 20 scans at b = 0 ms/µm^2, with TE = 42 ms, TR = 500 ms, δ = 5.5 ms, Δ = 12 ms, and an isotropic voxel size of 75 µm.

The human hippocampus was scanned at a 7T Bruker scanner with a transmit/receive volume resonator and using TR = 400 ms, TE = 40 ms, δ = 7 ms, Δ = 40 ms, 100 *q*-space directions (10 directions at b = 1ms/µm^2, 20 directions at b = 2 ms/µm^2, 30 directions at b = 5 ms/µm^2, 40 directions at b = 10 ms/µm^2) and 10 scans at b = 0 ms/µm^2.

For both datasets, after denoising and degibbsing [35,36], fiber responses and orientation distributions were computed using the *dwi2response* and *dwi2fod* functions in mrtrix3, using multi-tissue, multi-shell algorithms. These algorithms allow retrieval of fiber crossings detected by dMRI measurements. Fiber orientation distributions represented by sets of spherical harmonics are visualized using *mrview*.

3. Results

3.1. Validation with artificial crossings – SAXS detects up to three fibers down to 25° crossing angles

Analysis of the 2x-fiber configuration (Fig. 2A) shows that SAXS can recover crossing fiber populations. Strong fiber crossings are observed at most pixels in the overlapping region, with varying angles between the fibers in the two tissue strips. In general, the vertical strip shows fibers mostly running up-down (red color), with a weak horizontal component in the bottom half (pink). On the other hand, the horizontal strip seems to contain fibers that run almost exclusively left-right (cyan) and also many running left-right with an inclination of ∼30° (blue color). This is illustrated e.g. for point (i) in right panel of Fig. 2A, for which the azimuthal profile is plotted in Fig. 2B. At the middle-left of the overlapping region, the fibers seem to cross at almost 90° (Fig. 2A/B, point (ii)). In the upper part of the overlap region, fibers from the two strips seem to cross at angles ∼50° to 60° (cf Fig. 2A/B, point (iii)). While most crossings are resolved, there are small regions (e.g., in the lower and right parts of the overlapping area) where the angle between fibers decreases to the point where the two fiber populations become indistinguishable. The resolving limit for crossing angles is demonstrated in the 10 sub-sequent points highlighted with the yellow rectangle in Fig. 2A, for which the azimuthal profiles are displayed in Fig. 2C. Starting from the pixel #1 to the left, the angle between crossing fibers decreases from 30° to 26° (#2), while in pixels #3-7 the two peaks are not resolved by the algorithm (sensitivity of the algorithm is addressed in the Discussion). At pixels #8-10, the two separate fibers are detected again, with angles from 27° to 37°, respectively.

The 3x-fiber configuration (Fig. 2D) showcases the ability of SAXS to detect at least three crossing fiber tracts within a pixel. The fiber orientations from the 3 tissue strips have an average intersection angle of 60°, with the respective peaks clearly distinguishable, Fig. 2E. The majority of pixels in the region of overlap demonstrate 3 orientations, though in some regions only 2 crossing fibers are detected.

3.2. Mouse brain – detecting fiber crossings in myelinated areas

The mouse brain scanning SAXS data analysis using SLIX yielded a detailed fiber orientation map for the 25 µm-thin section

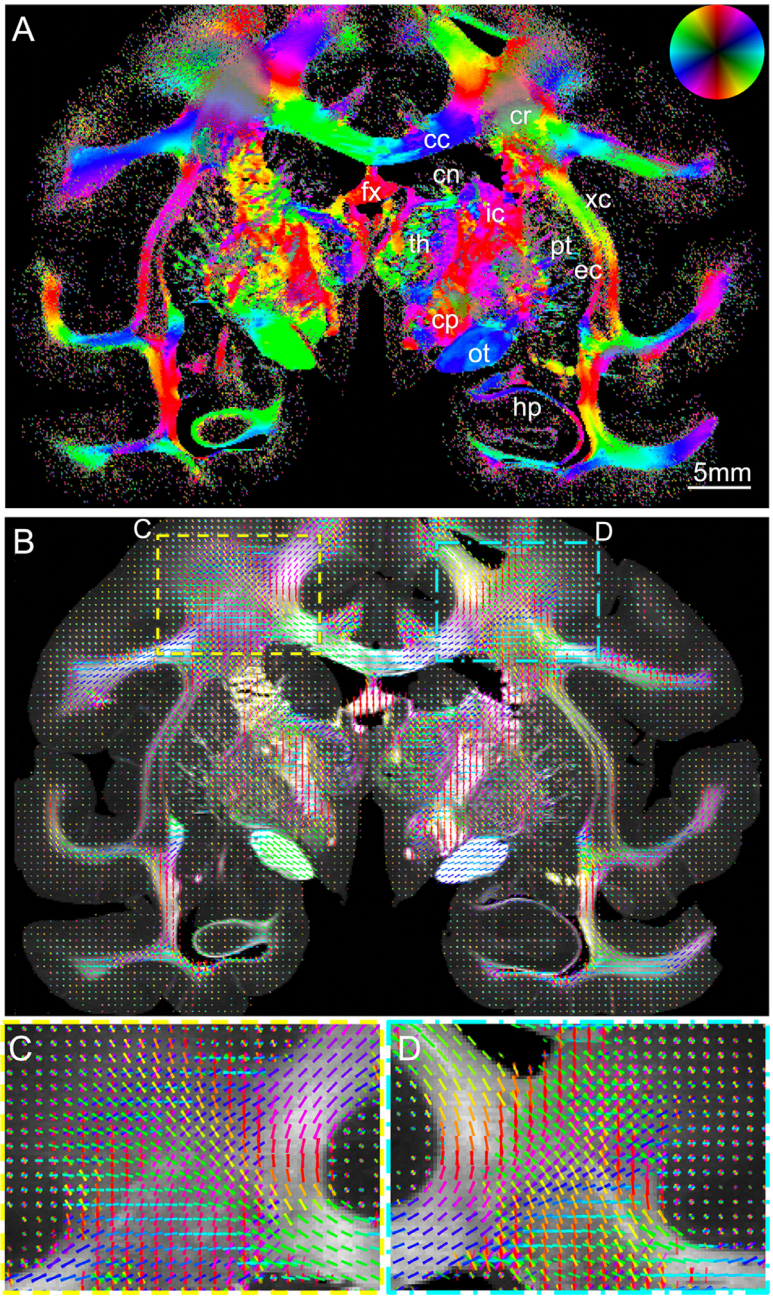

Fig. 5. SAXS-based fiber orientation analysis in a 60 μm-thick transverse section of a vervet monkey brain. (A) Fiber orientation map, with fiber orientations color-encoded according to the color wheel (using 4 quadrants per pixel as explained previously, so crossing fiber areas macroscopically appear gray, but individual colors can be resolved upon closer inspection). (B) Fiber orientations for the same section, represented by orientation-encoded colored bars for each 2×2 pixel set. (C-D) Enlarged views of the left and right corona radiata from the colored bar fiber orientation map in (B). cc: corpus callosum, cr: corona radiata, fx: fornix, cn: caudate nucleus, th: thalamus, ic: internal capsule, cp: cerebral peduncle, ot: optic tract, pt: putamen, ec: external capsule, xc: extreme capsule, hp: hippocampus.

(Fig. 3A), revealing intricate crossings in myelinated brain areas (e.g. Fig. 3A-iii). In the white matter, caudoputamen (CPu) fibers merge with the corpus callosum (cc), while some (white arrows) cross the lateral corpus callosum and the external capsule (ec) en route to the cortex, specifically the supplemental somatosensory area (SSs) (anatomic regions delineated on 3D-PLI in C-ii).

These crossings can also be inferred from the fiber tract trajectories seen using micrometer-resolution imaging of a section at a ~300 μm anterior plane from a different mouse with 3D-PLI (Fig. 3C, considering that 3D-PLI has limited sensitivity to crossing fibers within a pixel). They are more clearly visible in the axons seen by the tracer studies depicted in Fig. 3B, from the Allen Mouse Brain Connectivity Atlas [7] (https://connectivity.brain-map.org/), corresponding to experiments 297945448-SSs (Fig. 3B-ii) and 520728084-SSs (Fig. 3B-iii), which include injections in the supplemental somatosensory area. These axons can be clearly seen crossing primarily the lateral side of the corpus callosum and the external capsule to reach the caudoputamen.

On the other hand, such crossings might not be seen in visualizations of diffusion MRI data from the same region of the same mouse brain (Fig. 3D). For instance, Fig. 3D-ii shows a magnification of the same region as A-iii, B-ii/iii, C-ii, devoid of visible callosal crossings.

At the same time, crossings at the edge of the cortex, at the molecular layer, are also visible with scanning SAXS. There, myelinated fibers running circumferential to the brain surface to connect

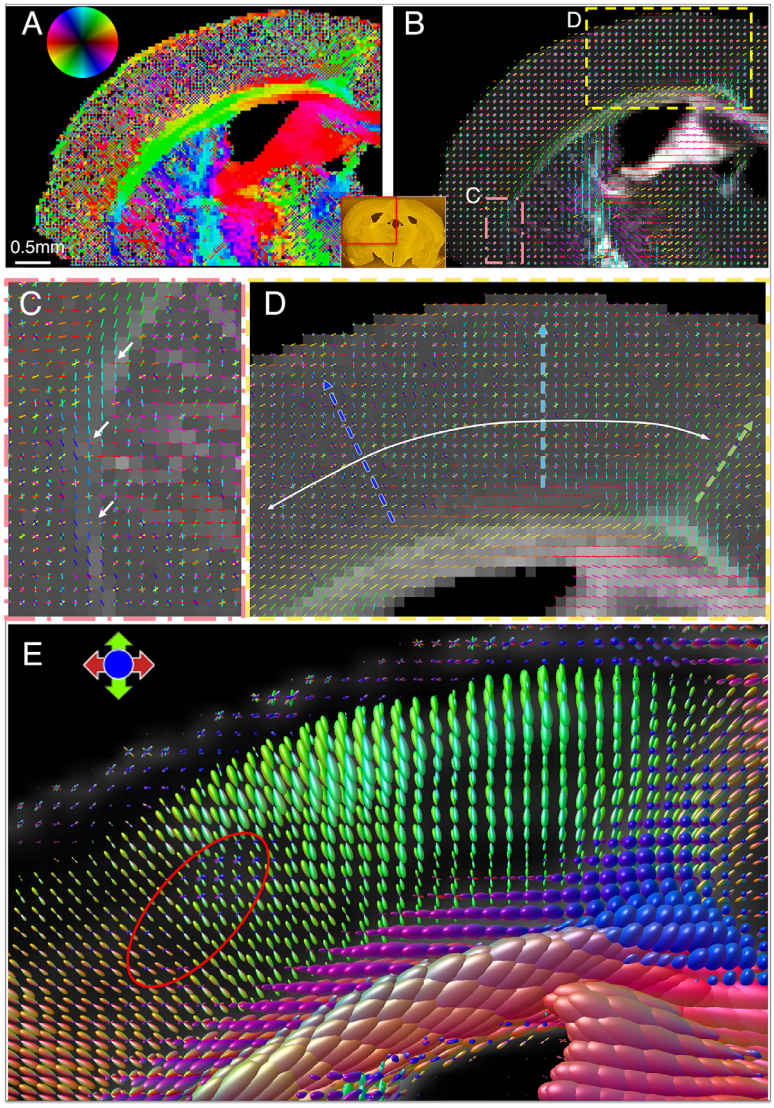

Fig. 6. SAXS-based analysis of crossing fibers in mouse cerebral cortex. (A-B) Fiber orientation maps of 50 µm-thick section, located ~200 µm anterior to section shown in Fig. 3 (section with scanned region in red rectangle shown in inset). (A) is color-encoded map (using 4 quadrants per pixel as explained in Section 2.3), with (B) being the corresponding color-coded bars representing fiber orientations overlaid on the scattering intensity map. C) Zoom-in of orange-red boxed region in (B), showing white matter fibers radiating from the internal capsule through the caudoputamen and crossing the external capsule fibers (in regions of white arrows) towards the lateral cortex. D) Enlarged view of yellow boxed region in (B), including part of the cortex, the corpus callosum and the cingulum. Fibers radiating out of each region of the corpus callosum towards the cortex, are depicted by the blue, cyan and green arrows. Orientation bars are shown in each pixel in C and D with the nominal image resolution (pixel dimension 50 µm). (E) Diffusion MRI zoomed-in fiber orientation map of the same region as (C), showing mainly the radial fibers (green). Some tangential fibers can also be identified (highlighted by the red ellipse).

to radial fibers of other cortical regions (yellow arrow in Fig. 3A-i). These circumferentially oriented axons are also visible in 3D-PLI (yellow arrow in Fig. 3C-i).

3.3. Pig brain – imaging complex fiber architectures in white matter

Contrary to the commonly studied lissencephalic rodent brain, the pig brain is gyrencephalic, meaning it has a folded structure containing gyri and sulci. This together with its bigger size results in a greater number of myelinated fibers with higher structural complexity of fiber tracts and multiple tract crossings (Fig. 4). The main regions of crossing fibers are enclosed in dotted boxes in Fig. 4B (labeled (i), (ii), and (iii)), and zoomed-in in Fig. 4C. The regions seem to be rich in 2x-fiber crossings, while some triple crossings can also be observed.

For instance, region (i) (cyan rectangle) contains callosal fibers from the lower left part at ~45° that curve rightwards or upwards (bottom left pair of white arrows), crossing with horizontally-traversing subcortical U-fibers (top arrow) and corticospinal fibers connecting to the internal capsule (bottom-right arrow). Similarly, in region (ii) (orange rectangle), the fibers entering from the left side (including callosal and subcortical U) or from right side (external capsule) cross with the numerous almost vertical corticospinal fibers from the internal capsule (vertical thick white arrow). Some corticospinal fibers from the superior frontal gyrus (bottom right curved arrow in i) appear to join this vertical portion of the internal capsule. Finally, in region (iii) (purple), another subcortical U-fiber population crosses with presumed callosal and internal capsule fibers.

3.4. Vervet brain – detecting crossings in challenging primate white matter geometries

The analysis of fiber orientations in the vervet brain section produced detailed maps of single and crossing fiber bundles (Fig. 5). Maps of the brain are seen in Fig. 5A-B, showing fiber

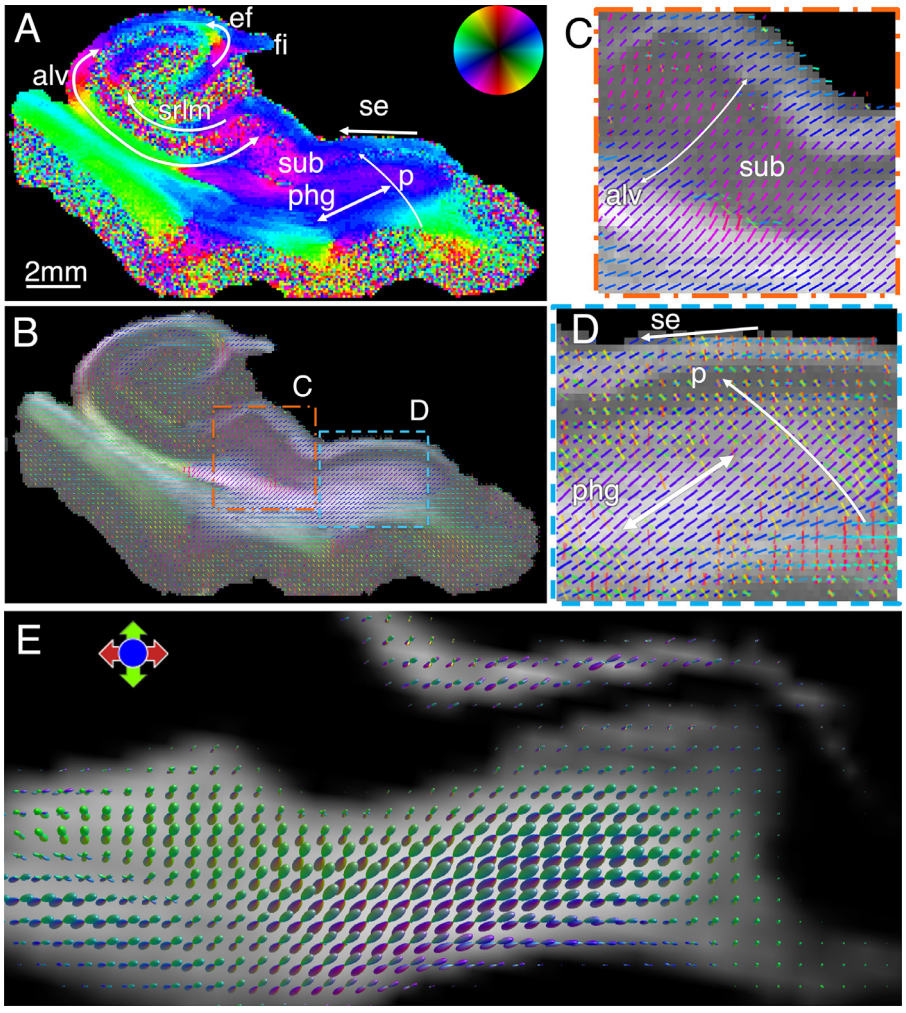

Fig. 7. Fiber orientation analysis in the human hippocampus. (A) SAXS fiber orientation map of a 75 µm section, with fiber orientations color-encoded according to the color wheel. (B) The same fiber orientations represented by orientation-encoded colored bars for each 2×2 pixel set. Only main orientation is depicted by adjusting the peak finding parameters (see text here and in Methods Section 2.3). (C) Zoomed-in image of the orange box in (B), showing forniceal tract (fo) fibers running through subiculum. (D) Zoomed-in image of the blue box in (B), depicting both primary and secondary fiber bundles in each pixel. (E) Diffusion MRI fiber orientations of region similar to (D), only showing orientations in white matter, without visible crossing perforant pathway fibers. p: perforant pathway, phg: parahipocampal gyral white matter, se: superficial entorhinal pathway, sub: subiculum, fo: forniceal path, srlm: stratum radiatum lacunosum and moleculare, ef: endfolial pathway, fi: fimbria.

bundles in the corpus callosum (cc), corona radiata (cr), fornix (fx), caudate nucleus (cn), thalamus (th), internal capsule (ic), cerebral peduncle (cp), optic tract (ot), putamen (pt), external capsule (ec), extreme capsule (xc), and hippocampus (hp). The regions with the most prominent crossing fiber populations are those in the corona radiata, Fig. 5C and D. There, at least two fiber populations cross, specifically the fibers radiating out of the corpus callosum (mostly left-right direction), and the fibers coming from the internal, external, and extreme capsules (mostly superior-inferior direction).

3.5. Pushing the limits: imaging gray matter crossings at the mouse cortex

The cortex is known to contain myelinated axons, with complex fiber architecture that can include crossings. Along these lines, apart from the crossings in primarily white matter regions shown in Fig. 3 and also depicted here in Fig. 6C, multiple crossings were also detected in the gray matter regions of the mouse brain. Fig. 6D displays part of the mouse cortex, where myelinated fibers radiate from the corpus callosum towards the periphery in all parts of the cortex. In addition, fibers are observed running through the cortex in a direction tangential to the corpus callosum (e.g. Fig. 6D, in mostly left-right direction, dashed colored arrows show the radial axon orientations, depicted by color-encoded lines).

Diffusion MRI can only in part recover these crossings using standard widely-used algorithms to retrieve fiber orientation distributions (see methods). For instance, Fig. 6E shows dMRI fiber orientation distributions from the same region of the same brain as in 6D. Fiber crossings can only be distinguished in part of the cortex (area of red ellipse).

3.6. Human hippocampus – detecting subtle secondary fiber tract crossings in human brain

The human hippocampus is a gray matter structure with numerous interwoven white matter pathways of immense complexity and importance to memory formation, which are altered in neurodegeneration and diseases such as Alzheimer's disease and epilepsy. Analysis of the human hippocampus section provided detailed maps of myelinated axon orientations across hippocampal subfields and the various hippocampal fiber tracts, as demonstrated in Fig. 7.

Fig. 7A shows the color-encoded main fiber orientation for each pixel (derived by adjusting SLIX parameters to only detect the main

peak in the line profiles, see Methods), revealing part of the complex anatomy of the hippocampus and the geometry of its fiber bundles. Primary fiber orientations are also depicted visually in Fig. 7B, in both white and gray matter areas. The main white matter tracts can be identified, including the alvear/forniceal (alv), perforant (p), stratum radiatum lacunosum and moleculare (srlm), endfolial (ef), and superficial entorhinal (se) pathways. Subicular fibers heading to/from the alveus (Fig. 7C) are also seen crossing the gray matter. In Fig. 7D, the cyan box in (B) is shown in higher resolution, demonstrating secondary and tertiary orientations of myelinated axons within white matter pixels. Multiple fiber orientations can be seen in most white matter pixels, meaning that in the complex hippocampal anatomy and connectivity, each pixel rarely contains fibers from a single bundle. For instance, the perforant pathway (p) is seen crossing the angular bundle within the parahippocampal gyrus (phg) just below the subiculum (sub) and reaching the superficial entorhinal (se) pathway within the stratum radiatum lacunosum and moleculare (srlm) – crossing the subicular forniceal bundle (alv) from 7C.

In contrast, analysis of diffusion MRI data of the same region (Fig. 7E) does not seem to recover these secondary orientations within the white matter voxels, which underlines the potential application of SAXS as an additional imaging modality to complement dMRI.

4. Discussion

In this study, we demonstrate the capability of SAXS to distinguish at least 3 distinct crossing fiber populations, at crossing angles as low as ~25°, and we show crossings in white and gray matter across different species. This separation is uncovered by analyzing the peaks in the azimuthal profiles from the scattering pattern of each scanned point, isolating the myelin signal corresponding to the periodicity of myelin. This work is a critical new direction to scanning SAXS capabilities shown previously, building upon the determination of main 3D fiber orientations in sections [22,26], and the comparison to MRI, quantification of myelin levels, orientation, and integrity in volumetric specimens [30].

4.1. Crossing angle detection limit

Given the experimental conditions and analysis tools presented in this study, the current limit of detection appears to be approximately 25°-30°. This angular resolving power depends on a few factors: first, the signal-to-noise ratio; if less photons impinge the sample, it is possible that noise in the azimuthal profiles could hamper peak detection. However, the current experiments with typical experimental conditions in scanning SAXS yield signals with a high signal-to-noise ratio, which are expected to be robust to such effects. Secondly, there is an inherent resolving limit to the method, which depends on the "fiber response function", i.e., the angular distribution of the signal arising from a single coherent, unidirectional fiber bundle. In theory, the SAXS signal from a single straight fiber would be exactly at 90° to the fiber orientation and have an azimuthal profile with two peaks of minimal width. However, in practice, myelinated axons have some curvature and undulations, and each pixel probed by the beam contains multiple fibers with a certain orientation distribution. Under these circumstances, the effective fiber response function has an azimuthal profile with a distribution similar to the peaks in Figs. 1 or 2. Taking these considerations as well as data from the current experiment into account, we speculate that the crossing angle detection (azimuthal resolution) could be lower at approximately 20°; possible improvements to the 25°-30° observed in this study might stem from higher signal-to-noise ratio experiments (i.e. using higher flux) or more sensitive peak detection algorithms, as discussed below. Finally, another case where crossing fibers can remain undetected is a scenario where the secondary fiber population contains considerably less myelinated axons (lower number of axons, or axons with a lower degree of myelination). In that case, its scattering peak might not be detected, unless the signal-to-noise ratio is very high, or a micrometer-resolution scan can visually resolve the myelinated axons contained in different tracts. Such resolution can be attained by decreasing beam diameter and motor step size (see Section 4.4 for more discussion on resolution), or by use of other orientation-sensitive microscopy methods, such as scattered light imaging [18,31,33].

4.2. Comparison to diffusion MRI and other methods

We show that SAXS can recover crossings, which sometimes cannot be retrieved using diffusion MRI, in white and gray matter, in both animal and human brain tissue. This capability can be attributed to the distinct characteristics of SAXS compared to other methods. Scanning SAXS has different advantages and shortcomings compared to the multiple other methods employed towards detecting fiber orientations and crossing fibers in the animal and human brain. Since diffusion MRI is the only modality which can be applied both *in vivo* and *ex vivo* with minimal sample preparation, other methods aim to overcome its shortcomings.

Limitations of diffusion MRI mostly stem from the fact that it uses the directional movement of water molecules as a proxy for fiber orientation. As a result, (i) it is difficult to translate findings from *ex vivo* to *in vivo*, since water content and motility are altered in fixed samples; (ii) movement of water is also restricted or hindered by all structures in the brain [37], including membranes of other cells, organelles, extracellular matrix and vesicles, cell cytoskeleton, vesicle walls, while water can passively or actively move across membranes [38]; (iii) fiber response function is inherently broader compared to SAXS, because even in the case of perfectly aligned fiber population, all the above factors, as well as the movement of water in random directions (to the extent allowed) within the neuronal somata, axons, other brain cells, and in the extracellular space, contribute to an angular dispersion of the signal. In addition, dMRI resolution is typically restricted to hundreds of micrometers per voxel, potentially corresponding to thousands of fibers, further contributing to the angular dispersion. Moreover, different data processing and visualization algorithms can provide differing fiber orientation distributions from the same dMRI data. All these make interpretation of diffusion MRI output very challenging and emphasize the need for validation methods [21].

As described, the main limitation of dMRI is lack of specificity to myelinated axons. In contrast, this specificity can be provided by scanning SAXS, confocal/multi-photon microscopy (possibly combined with clearing), and polarization-based methods (3D-PLI/PS-OCT). The limitation of polarization-based methods is that they are performed on 2D samples (sections or surfaces). Confocal/multi-photon microscopy without clearing is limited in depth, and different antibodies can yield different results, depending on the origin of the tissue, sample preparation method etc., whereas clearing is labor and time-intensive, typically resulting in tissue deformation, and is challenging for large specimens. SAXS on the other hand does not depend on staining given its specificity to myelin nanostructure, and X-rays can penetrate thick specimens. Here, we are only studying tissue slices using SAXS. Future implementations of SAXS tensor tomography with crossing fiber detection may provide specificity across a tissue volume.

Another limitation of dMRI is its resolution, which is limited to hundreds of micrometers. Methods such as 3D-PLI, SLI, and PS-OCT can reach micrometer resolutions, since each image pixel contains orientation information, with SLI also being able to detect cross-

ings in each pixel, while 3D-PLI and PS-OCT depend on their high resolution for visually resolving crossings. Analysis of brightfield or fluorescence images using structure tensor to derive fiber orientations based on intensity gradients can provide resolution of few to several tens of micrometers, depending on the kernel size used. Of the microscopy techniques, electron microscopy currently provides the highest resolution, achieving sub-nanometer resolutions, but the field of view is typically less than a millimeter, and sample preparation is extensive and usually tissue-distorting. Finally, scanning SAXS orientation analysis can reach sub-micrometer resolutions [39,40], depending on the beamsize and motor step size used, and crossings can be detected for each pixel (also see Section 4.4 for more discussion on SAXS resolution and its limits).

Another notable advantage of scanning SAXS versus other MRI validation methods is its ability to provide quantitative 3D orientations in isotropic voxels, both tomographically and in sections. Brightfield methods are only 2D, while 3D fluorescence imaging has a lower through-plane compared to in-plane resolution, and structure tensor analysis is challenging in dense white matter regions where intensity gradients are low. 3D-PLI can also provide 3D orientation, but the out-of-plane angle can be ambiguous, while SLI yields information on out-of-plane angles, but quantification has not yet been achieved.

Finally, tensor tomographic SAXS [28–30] is the only method together with MRI that allows studying intact specimens in a fully 3D manner. Nonetheless, tomographic reconstruction of crossing fibers still requires theoretical and methodological advances, which the community is currently working on. Beside, methods based on optical photons are limited by low penetration depth due to photon scattering and therefore used for studying tissue sections. Tissue clearing circumvents the scattering problem by making the tissue transparent and thus also enables 3D imaging of specimens. However, the tissue is usually distorted by the clearing process, and samples larger than few millimeters pose challenges in clearing, antibody penetration for staining, and imaging. Currently, specimens as thick as 20mm have been scanned using SAXS-TT [30]. It is worth noting that SAXS tensor tomography scanning of bulk samples can be limited by absorption of scattered photons by the samples, restricting the possible sample sizes. However, it might be possible to counteract the absorption effects by using higher photon energies. This will have to be balanced against the lower incidence of scattering events occurring with higher energy photons and the possibility of multiple scattering events in a larger sample volume. The limits of the sample size that can be scanned tomographically using SAXS tensor tomography remain to be determined.

4.3. Fiber crossings in white and gray matter from multiple species

We have demonstrated the capability of SAXS to identify fiber crossings in the brains of various species. In mouse brain, fiber crossings in both white and gray matter have been revealed. White matter crossings were seen mostly involving fibers originating in the cortex and crossing the corpus callosum, and external capsule on their way to the caudoputamen. The relative scarcity of white matter crossings is expected given the relative simplicity of the rodent brain compared to gyrencephalic brains. Nevertheless, X-ray scattering was also able to distinguish crossings of myelinated axons within gray matter regions, including tangential fibers crossing the more abundant radial ones [41]. This was only previously reported using tracer studies [7], special very-high-resolution microscopy methods [42], or very high angular and spatial resolution diffusion MRI [41,43].

We have also investigated fiber crossings in a Yucatan micropig brain. Since the pig brain is increasingly used in neuroscientific studies [44], including studies of white matter and structural connectivity [45,46], it is essential that the white matter fiber orientations are studied and accurately mapped. In addition, the swine model is often used in biomechanical studies [47], where axonal orientation seems to play a role for axonal injury and for computational determination of local mechanical strains [48]. Biomechanical implications of crossing fibers have not been adequately studied to date, so combined imaging and mechanical experiments could help elucidate the structure-biomechanics relationship.

The primate (vervet monkey) brain exhibits similar architecture to the human brain, which makes it highly suitable for neuroscientific studies [49] addressing both structural [50] and functional aspects [51]. Beside, most knowledge of gold-standard human connectivity comes from tracer studies in primates [8,52,53]. 3D-PLI of vervet monkey brain regions has provided fiber orientations maps at micrometer resolution [50], while SLI has also enabled discerning of crossing nerve fibers at such resolution [18,31,33]. Our scanning SAXS maps provide detailed fiber crossing information across the vervet monkey brain section. The corona radiata SAXS maps appear similar to corona radiata SLI maps [18,33]. Combining the specificity to myelinated axons of SAXS with the high-resolution capabilities of SLI can potentially help to solve long-standing fiber orientation and tractography issues in brain connectivity, such as the high false-positivity rates of tractography algorithms [54,55], or the challenges posed in complex fiber geometry regions where multiple fiber bundles combine and have in/through-plane trajectories [55,56].

The human hippocampus is critical for new memory formation, and shows degraded function in neurodegenerative diseases such as Alzheimer's disease (AD) [57]. However, its location towards the lower part of the brain, next to the mastoid air cells, its complex anatomy [58] and connectivity [59] as well as its relatively small size, makes it challenging to study with MRI [60], which is the most commonly used *in vivo* brain imaging modality. Nevertheless, the significance of the hippocampus has prompted multiple approaches to study its anatomy and connectivity in detail. *In vivo* MRI studies have been able to segment the hippocampal subfields [61], and reveal the main and even microscopic fiber pathways [62,63]. *Ex vivo*, high-resolution MRI has been commonly used to study hippocampal connectivity in excised specimens; early high-resolution anatomical and diffusion tensor imaging scanning could delineate the different laminae [64]. Modern scanners and approaches combining scanning with histology can also yield detailed subfield segmentation and studies in the context of neurodegenerative diseases [65,66]. In addition, micrometer-resolution scanning using polarized light imaging has allowed unprecedented insights into the hippocampal connectivity [15]. Here, we have shown myelinated-axon-specific maps of fiber orientations using X-ray scattering in a human hippocampal specimen, including dominant and secondary fiber pathways in white and gray matter. Such information could potentially reveal a loss of normal white matter pathways in neurodegenerative diseases, where demyelination has been observed, as well as loss of specific pathways such as the perforant pathways in AD. Combining this approach with increasing data at the histopathologic [67], cytomolecular [68], as well as transcriptomic [69,70] and genetic [71] levels could help investigate the role of myelin and oligodendrocytes in the context of disease mechanisms.

4.4. Limitations

The study has a number of limitations. First, the ground truth for fiber orientations constitutes an ongoing challenge. We attempted to overcome this by (i) validating against strips of unidirectional fibers artificially superimposed to mimic pixels with crossings, noting that scanning SAXS has been demonstrated in brain tissue for primary orientation [22,30], and (ii) comparing

SAXS data to a micrometer-resolution 3D-PLI image of a similar region of a mouse brain. However, even in the artificial crossings using corpus callosum strips, fibers are not fully aligned within each strip, so ground-truth crossing angles cannot be exactly determined. On the other hand, SAXS yields directional information from myelinated axons directly and with specificity, so the fiber orientations are relatively easily and directly interpreted compared to structural imaging or diffusion MRI, where myelinated-axon-specific orientation analyses include more complex algorithms and more assumptions.

In terms of diffusion MRI analysis, we used standard orientation calculation and visualization methods, and specific scanning protocols. It is conceivable that some crossing fibers that are missed in this study might have been recovered by using alternative methods. However, we utilize the most commonly used tools for fiber orientation retrieval from diffusion MRI data. Similarly, processing of the SAXS signal is also done using readily available fiber orientation determination tools (the SLIX software in that case). As such, we consider the head-to-head comparison to be fair.

SAXS scans can achieve a moderately high resolution while discerning crossing fibers. The highest resolution demonstrated here was for the first mouse brain section, with a pixel size of 25 micrometers, whereas resolution was 125 micrometers for the vervet brain – much lower than the resolution typically reached in 3D-PLI or SLI. Although SAXS scanning can be performed at very high resolutions, down to sub-micrometer levels [40], practical considerations (beamline capabilities regarding beamsize, and the time needed for raster-scanning an extended field of view at such resolutions) limit the resolution to typically tens of micrometers. This is below or at the same order as that of diffusion MRI, with the advantage of specificity to the myelinated fibers, rendering scanning SAXS a very good validation tool for dMRI on similarly-sized samples.

Sensitivity to peak detection in the azimuthal profiles presents a challenge for future improvements. In this study, the SLIX software [32] used the SAXS azimuthal profile data as input. SLIX was developed for SLI data, where, similar to SAXS, photons also scatter anisotropically off the sample depending on the orientation of its microstructure. In both methods, the position of the peaks in azimuthal profiles reveals the in-plane orientation of the fibers. Yet, improvement appears feasible: the azimuthal profiles of pixels 3, 6, and 7 in Fig. 2 suggest the presence of two peaks that are at an angle of $\sim 20^\circ$ apart. This could indicate that a more sensitive peak-fitting algorithm, the subject of our future work, could possibly be able to tell these peaks apart, thus resolving even lower angle crossings.

When it comes to tissue preparation for imaging, the scanning SAXS experiments described here were performed on thin sections. Although this is a very common approach used in histology or methods such as 3D-PLI or SLI, in many cases, sectioning the sample is not desired, or not feasible. However, with the advent of SAXS tensor tomography [28,30], such experiments can also be performed tomographically on whole specimens without sectioning. The challenge of computing both the tensor-tomographic reconstruction and depicting multiple fiber orientations per voxel will also be the subject of future investigations. This would provide a tomographic gold-standard in the axonal orientation field and enable a head-to-head validation of diffusion MRI orientation information on the same specimens.

Access to scanning SAXS is also a limitation since the required photon flux of micro-focused beam is currently only obtainable from synchrotrons. Yet, several sites worldwide provide appropriate beamlines for collaborative use. Continued improvement of instrumentation and analysis will enable higher sample throughput as well as scanning SAXS experiments on lab SAXS setups.

Finally, biological damage by ionizing power radiation is a concern when using high-intensity X-rays. For this reason, both the instantaneous and the total X-ray doses in a SAXS experiment need to be carefully controlled by selecting the proper beam filters and exposure time. We have tried to do that in our present as well as in our past experiments, including in tomography mode. As a result, we have not observed significant changes in the sample (ultra) structure (e.g. [30], Supplementary Fig. 7) and have also confirmed that subsequent downstream processing (e.g., histology or immunohistochemistry, e.g. [30], Fig. 5 and Supplementary Fig. 7) has been unaffected by our scanning (to the extent that could be observed by comparison to non-scanned samples). Hence, changes might be limited to scales below the ones relevant for investigations such as in this study. It should be noted though that the doses deposited on the samples are beyond the ones allowed for live animal imaging. Therefore, possible application of 2D or 3D SAXS for fiber orientation determination *in vivo* might have to use a combination of lower resolution and sparse sampling approaches to reduce sample exposure.

5. Conclusion

Accurate and specific imaging of crossing nerve fibers is an important challenge in connectomics and neuroscience. In the experiments presented here, we use scanning small-angle X-ray scattering (SAXS) to show that detecting crossing fibers is feasible for at least three crossing fiber bundles and crossing angles down to approximately 25°. We have applied the method across several mammalian species – in mouse, pig, vervet monkey, and human brain, studying both gray and white matter. Overall, as scanning SAXS can provide specificity to myelinated axonal orientations, which are responsible for long-distance signal transmission in the brain, it has the potential to become a reference method for accurate fiber orientation mapping. Combination of scanning SAXS with micrometer-resolution imaging approaches, such as 3D-PLI or SLI, taking advantage of SAXS's specificity and 3D-PLI/SLI resolution, could provide ground truth information on fiber orientations, yield more accurate structural connectivity maps and potentially provide the basis for validation of diffusion MRI signals.

Data statement

SAXS data for all samples are deposited at: 10.5281/zenodo.7228131

Declaration of Competing Interest

The authors declare that they have no known competing financial interests or personal relationships that could have appeared to influence the work reported in this paper.

Acknowledgments

We thank all animal and human donors. We also thank Samuel Baker from Stanford Comparative Medicine, Roger Woods from the UCLA Brain Research Institute and Donald Born from Stanford Neuropathology for providing the pig, vervet and human brain samples respectively. The present work was supported by the National Institutes of Health (NIH), award numbers R01NS088040, P41EB017183, R01AG061120-01, R01MH092311, and 5P40OD010965, and by the European Union's Horizon 2020 Research and Innovation Programme under Grant Agreement No. 945539 ("Human Brain Project" SGA3). 3D-PLI images were generated by utilizing the computing time granted through JARA-HPC on the supercomputer JURECA at Forschungszentrum Juelich (FZJ), Germany. SSRL, SLAC National Accelerator Laboratory, is supported

by the U.S. Department of Energy, under Contract No. DE-AC02-76SF00515. The SSRL Structural Molecular Biology Program is supported by the DOE Office of Biological and Environmental Research, and by the National Institutes of Health, National Institute of General Medical Sciences (P30GM133894). The Pilatus detector at beamline 4-2 at SSRL was funded under National Institutes of Health Grant S10OD021512. The experiment on mouse brain sections were carried out at the cSAXS beamline, Swiss Light Source, Paul Scherrer institute, Switzerland, and the artificial crossings, pig, vervet and human sections in the 4-2 beamline of Stanford Synchrotron Radiation Lightsource, SLAC National Laboratory, USA.

References

[1] P. Morell, Myelin, 2nd ed., Springer Science+Business Media, New York, 1984, doi:10.1007/978-1-4757-1830-0.
[2] O. Sporns, G. Tononi, R. Kötter, The human connectome: a structural description of the human brain, PLoS Comput Biol 1 (4) (2005) e42, doi:10.1371/journal.pcbi.0010042.
[3] P. Hagmann, From diffusion MRI to brain connectomics, EPFL (2005).
[4] F.A.C. Azevedo, L.R.B. Carvalho, L.T. Grinberg, J.M. Farfel, R.E.L. Ferretti, R.E.P. Leite, W.J. Filho, R. Lent, S. Herculano-Houzel, Equal numbers of neuronal and nonneuronal cells make the human brain an isometrically scaled-up primate brain, J. Comp. Neurol. 513 (5) (2009) 532–541, doi:10.1002/cne.21974.
[5] Y. Tang, J.R. Nyengaard, A stereological method for estimating the total length and size of myelin fibers in human brain white matter, J. Neurosci. Methods 73 (2) (1997) 193–200, doi:10.1016/S0165-0270(97)02228-0.
[6] A. Peters, S.L. Palay, H.F. Webster, The Fine Structure of the Nervous System. Neurons and their Supporting Cells, 3rd ed., Oxford University Press, New York, 1991.
[7] S.W. Oh, J.A. Harris, L. Ng, B. Winslow, N. Cain, S. Mihalas, Q. Wang, C. Lau, L. Kuan, A.M. Henry, M.T. Mortrud, B. Ouellette, T.N. Nguyen, S.A. Sorensen, C.R. Slaughterbeck, W. Wakeman, Y. Li, D. Feng, A. Ho, E. Nicholas, K.E. Hirokawa, P. Bohn, K.M. Joines, H. Peng, M.J. Hawrylycz, J.W. Phillips, J.G. Hohmann, P. Wohnoutka, C.R. Gerfen, C. Koch, A. Bernard, C. Dang, A.R. Jones, H. Zeng, A mesoscale connectome of the mouse brain, Nature 508 (2014) 207, doi:10.1038/nature13186.
[8] N.T. Markov, M.M. Ercsey-Ravasz, A.R. Ribeiro Gomes, C. Lamy, L. Magrou, J. Vezoli, P. Misery, A. Falchier, R. Quilodran, M.A. Gariel, J. Sallet, R. Gamanut, C. Huissoud, S. Clavagnier, P. Giroud, D. Sappey-Marinier, P. Barone, C. Dehay, Z. Toroczkai, K. Knoblauch, D.C. Van Essen, H. Kennedy, A weighted and directed interareal connectivity matrix for macaque cerebral cortex, Cereb. Cortex 24 (1) (2014) 17–36 Jan, doi:10.1093/cercor/bhs270.
[9] J.A. Harris, S. Mihalas, K.E. Hirokawa, J.D. Whitesell, H. Choi, A. Bernard, P. Bohn, S. Caldejon, L. Casal, A. Cho, A. Feiner, D. Feng, N. Gaudreault, C.R. Gerfen, N. Graddis, P.A. Groblewski, A.M. Henry, A. Ho, R. Howard, J.E. Knox, L. Kuan, X. Kuang, J. Lecoq, P. Lesnar, Y. Li, J. Luviano, S. McConoughey, M.T. Mortrud, M. Naeemi, L. Ng, S.W. Oh, B. Ouellette, E. Shen, S.A. Sorensen, W. Wakeman, Q. Wang, Y. Wang, A. Williford, J.W. Phillips, A.R. Jones, C. Koch, H. Zeng, Hierarchical organization of cortical and thalamic connectivity, Nature 575 (7781) (2019) 195–202, doi:10.1038/s41586-019-1716-z.
[10] H. Hintiryan, N.N. Foster, I. Bowman, M. Bay, M.Y. Song, L. Gou, S. Yamashita, M.S. Bienkowski, B. Zingg, M. Zhu, X.W. Yang, J.C. Shih, A.W. Toga, H.W. Dong, The mouse cortico-striatal projectome, Nat. Neurosci. 19 (8) (2016) 1100–1114, doi:10.1038/nn.4332.
[11] W. Möbius, K.A. Nave, H.B. Werner, Electron microscopy of myelin: structure preservation by high-pressure freezing, Brain Res. 1641 (2016) 92–100, doi:10.1016/j.brainres.2016.02.027.
[12] L.J. Hogstrom, S.M. Guo, K. Murugadoss, M. Bathe, Advancing multiscale structural mapping of the brain through fluorescence imaging and analysis across length scales, Interface Focus 6 (1) (2016) 20150081 Feb, doi:10.1098/rsfs.2015.0081.
[13] K. Chung, K. Deisseroth, CLARITY for mapping the nervous system, Nat. Methods 10 (6) (2013) 508–513, doi:10.1038/nmeth.2481.
[14] M. Axer, K. Amunts, D. Grässel, C. Palm, J. Dammers, H. Axer, U. Pietrzyk, K. Zilles, A novel approach to the human connectome: ultra-high resolution mapping of fiber tracts in the brain, Neuroimage 54 (2) (2011) 1091–1101, doi:10.1016/j.neuroimage.2010.08.075.
[15] M.M. Zeineh, N. Palomero-Gallagher, M. Axer, D. Grassel, M. Goubran, A. Wree, R. Woods, K. Amunts, K. Zilles, Direct visualization and mapping of the spatial course of fiber tracts at microscopic resolution in the human hippocampus, Cereb. Cortex 27 (3) (2017) 1779–1794, doi:10.1093/cercor/bhw010.
[16] H. Wang, J. Zhu, M. Reuter, L.N. Vinke, A. Yendiki, D.A. Boas, B. Fischl, T. Akkin, Cross-validation of serial optical coherence scanning and diffusion tensor imaging: A study on neural fiber maps in human medulla oblongata, Neuroimage 100 (2014) 395–404, doi:10.1016/j.neuroimage.2014.06.032.
[17] R. Jones, G. Grisot, J. Augustinack, C. Magnain, D.A. Boas, B. Fischl, H. Wang, A. Yendiki, Insight into the fundamental trade-offs of diffusion MRI from polarization-sensitive optical coherence tomography in *ex vivo* human brain, Neuroimage 214 (2020) 116704, doi:10.1016/j.neuroimage.2020.116704.
[18] M. Menzel, J.A. Reuter, D. Gräßel, M. Huwer, P. Schlömer, K. Amunts, M. Axer, Scattered light imaging: resolving the substructure of nerve fiber crossings in whole brain sections with micrometer resolution, Neuroimage 233 (2021) 117952, doi:10.1016/j.neuroimage.2021.117952.
[19] H. Johansen-Berg, M.F. Rushworth, Using diffusion imaging to study human connectional anatomy, Annu. Rev. Neurosci. 32 (2009) 75–94, doi:10.1146/annurev.neuro.051508.135735.
[20] B.J. Jellison, A.S. Field, J. Medow, M. Lazar, M.S. Salamat, A.L. Alexander, Diffusion tensor imaging of cerebral white matter: a pictorial review of physics, fiber tract anatomy, and tumor imaging patterns, Am. J. Neuroradiol. 25 (3) (2004) 356–369 [Online]. Available: internal-pdf://64.120.241.21/review_2004_Jellison_DTI of Cerebral WM%3B A Pic.pdf.
[21] A. Yendiki, M. Aggarwal, M. Axer, A.F.D. Howard, A.-M. van C. van Walsum, S.N. Haber, Post mortem mapping of connectional anatomy for the validation of diffusion MRI, Neuroimage 256 (2022) 119146, doi:10.1016/j.neuroimage.2022.119146.
[22] M. Georgiadis, A. Schroeter, Z. Gao, M. Guizar-Sicairos, D.S. Novikov, E. Fieremans, M. Rudin, Retrieving neuronal orientations using 3D scanning SAXS and comparison with diffusion MRI, Neuroimage 204 (2020) 116214, doi:10.1016/j.neuroimage.2019.116214.
[23] R. Ashkar, H.Z. Bilheux, H. Bordallo, R. Briber, D.J.E. Callaway, X. Cheng, X.-Q. Chu, J.E. Curtis, M. Dadmun, P. Fenimore, D. Fushman, F. Gabel, K. Gupta, F. Herberle, F. Heinrich, L. Hong, J. Katsaras, Z. Kelman, E. Kharlampieva, G.R. Kneller, A. Kovalevsky, S. Krueger, P. Langan, R. Lieberman, Y. Liu, M. Losche, E. Lyman, Y. Mao, J. Marino, C. Mattos, F. Meilleur, P. Moody, J.D. Nickels, W.B. O'Dell, H. O'Neill, U. Perez-Salas, J. Peters, L. Petridis, A.P. Sokolov, C. Stanley, N. Wagner, M. Weinrich, K. Weiss, T. Wymore, Y. Zhang, J.C. Smith, Neutron scattering in the biological sciences: progress and prospects, Acta Crystallogr. Sect. D 74 (12) (2018) 1129–1168 Dec, doi:10.1107/S2059798318017503.
[24] F. Natali, C. Dolce, J. Peters, C. Stelletta, B. Demé, J. Ollivier, M. Boehm, G. Leduc, I. Piazza, A. Cupane, E.L. Barbier, Anomalous water dynamics in brain: a combined diffusion magnetic resonance imaging and neutron scattering investigation, J. R. Soc. Interface 16 (157) (2019) 20190186 Aug, doi:10.1098/rsif.2019.0186.
[25] S. Maiti, H. Frielinghaus, D. Gräßel, M. Dulle, M. Axer, S. Förster, Distribution and orientation of nerve fibers and myelin assembly in a brain section retrieved by small-angle neutron scattering, Sci. Rep. 11 (1) (2021) 17306, doi:10.1038/s41598-021-92995-2.
[26] M. Georgiadis, M. Guizar-Sicairos, A. Zwahlen, A.J. Trüssel, O. Bunk, R. Müller, P. Schneider, 3D scanning SAXS: A novel method for the assessment of bone ultrastructure orientation, Bone 71 (0) (2015) 42–52, doi:10.1016/j.bone.2014.10.002.
[27] M. Georgiadis, M. Guizar-Sicairos, O. Gschwend, P. Hangartner, O. Bunk, R. Muller, P. Schneider, Ultrastructure organization of human trabeculae assessed by 3D sSAXS and relation to bone microarchitecture, PLoS One 11 (8) (2016) e0159838, doi:10.1371/journal.pone.0159838.
[28] M. Liebi, M. Georgiadis, A. Menzel, P. Schneider, J. Kohlbrecher, O. Bunk, M. Guizar-Sicairos, Nanostructure surveys of macroscopic specimens by small-angle scattering tensor tomography, Nature 527 (7578) (2015) 349–352, doi:10.1038/nature16056.
[29] M. Liebi, M. Georgiadis, J. Kohlbrecher, M. Holler, J. Raabe, I. Usov, A. Menzel, P. Schneider, O. Bunk, M. Guizar-Sicairos, Small-angle X-ray scattering tensor tomography: model of the three-dimensional reciprocal-space map, reconstruction algorithm and angular sampling requirements, Acta Crystallogr. A Found. Adv. 74 (Pt 1,) (2018) 12–24, doi:10.1107/s205327331701614x.
[30] M. Georgiadis, A. Schroeter, Z. Gao, M. Guizar-Sicairos, M. Liebi, C. Leuze, J.A. McNab, A. Balolia, J. Veraart, B. Ades-Aron, S. Kim, T.M. Shepherd, C.H. Lee, P. Walczak, S. Chodankar, P. DiGiacomo, G. David, M. Augath, V. Zerbi, S. Sommer, I. Rajkovic, T. Weiss, O. Bunk, L. Yang, J. Zhang, D.S. Novikov, M. Zeineh, E. Fieremans, M. Rudin, Nanostructure-specific X-ray tomography reveals myelin levels, integrity and axon orientations in mouse and human nervous tissue, Nat. Commun. 12 (2941) (2021), doi:10.1038/s41467-021-22719-7.
[31] M. Menzel, M. Axer, H. De Raedt, I. Costantini, L. Silvestri, F.S. Pavone, K. Amunts, K. Michielsen, Toward a high-resolution reconstruction of 3D nerve fiber architectures and crossings in the brain using light scattering measurements and finite-difference time-domain simulations, Phys. Rev. X 10 (2) (2020) 21002 Apr, doi:10.1103/PhysRevX.10.021002.
[32] J.A. Reuter, M. Menzel, SLIX: A Python package for fully automated evaluation of Scattered Light Imaging measurements on brain tissue, J. Open Source Softw. 5 (54) (2020) 2675.
[33] M. Menzel, M. Ritzkowski, J.A. Reuter, D. Gräßel, K. Amunts, M. Axer, Scatterometry measurements with scattered light imaging enable new insights into the nerve fiber architecture of the brain, Front. Neuroanat. 15 (2021) [Online]. Available https://www.frontiersin.org/articles/10.3389/fnana.2021.767223.
[34] M. Stacho, C. Herold, N. Rook, H. Wagner, M. Axer, K. Amunts, O. Güntürkün, A cortex-like canonical circuit in the avian forebrain, Science 369 (6511) (Sep. 2020) eabc5534 80-., doi:10.1126/science.abc5534.
[35] B. Ades-Aron, J. Veraart, P. Kochunov, S. McGuire, P. Sherman, E. Kellner, D.S. Novikov, E. Fieremans, Evaluation of the accuracy and precision of the diffusion parameter EStImation with Gibbs and NoisE removal pipeline, Neuroimage 183 (2018) 532–543, doi:10.1016/j.neuroimage.2018.07.066.
[36] J. Veraart, D.S. Novikov, D. Christiaens, B. Ades-aron, J. Sijbers, E. Fieremans, Denoising of diffusion MRI using random matrix theory, Neuroimage 142 (2016) 394–406 Supplement C, doi:10.1016/j.neuroimage.2016.08.016.
[37] C. Beaulieu, The basis of anisotropic water diffusion in the nervous system–a technical review, NMR Biomed. 15 (7-8) (2002) 435–455.

[38] N. MacAulay, Molecular mechanisms of brain water transport, Nat. Rev. Neurosci. 22 (6) (2021) 326–344, doi:10.1038/s41583-021-00454-8.
[39] H. Inouye, J. Liu, L. Makowski, M. Palmisano, M. Burghammer, C. Riekel, D.A. Kirschner, Myelin organization in the nodal, paranodal, and juxtaparanodal regions revealed by scanning x-ray microdiffraction, PLoS One 9 (7) (2014) e100592, doi:10.1371/journal.pone.0100592.
[40] H. Inouye, F.-H. Kuo, A.R. Denninger, B. Weinhausen, M. Burghammer, D.A. Kirschner, Myelin structure in unfixed, single nerve fibers: Scanning X-ray microdiffraction with a beam size of 200nm, J. Struct. Biol. (2017), doi:10.1016/j.jsb.2017.07.001.
[41] O.F. Gulban, F. De Martino, A.T. Vu, E. Yacoub, K. Uğurbil, C. Lenglet, Cortical fibers orientation mapping using *in-vivo* whole brain 7 T diffusion MRI, Neuroimage 178 (2018) 104–118 Sep, doi:10.1016/j.neuroimage.2018.05.010.
[42] M.J. Redlich, H. Lim, A Method to measure myeloarchitecture of the murine cerebral cortex *in vivo* and *ex vivo* by intrinsic third-harmonic generation, Front. Neuroanat. 13 (2019) 65 Jun, doi:10.3389/fnana.2019.00065.
[43] C.W.U. Leuze, A. Anwander, P.L. Bazin, B. Dhital, C. Stüber, K. Reimann, S. Geyer, R. Turner, Layer-specific intracortical connectivity revealed with diffusion MRI, Cereb. Cortex 24 (2) (2014) 328–339 Feb, doi:10.1093/cercor/bhs311.
[44] N.M. Lind, A. Moustgaard, J. Jelsing, G. Vajta, P. Cumming, A.K. Hansen, The use of pigs in neuroscience: Modeling brain disorders, Neurosci. Biobehav. Rev. 31 (5) (2007) 728–751, doi:10.1016/j.neubiorev.2007.02.003.
[45] R.A. Benn, R.B. Mars, T. Xu, J.R. Yee, L. Rodríguez-Esparragoza, P. Montesinos, J.P. Manzano-Patron, G. Lopez-Martin, V. Fuster, J. Sanchez-Gonzalez, E.P. Duff, and B. Ibañez, "Opening the pig to comparative neuroimaging: a common space approach contextualizes the pig and human structural connectome," bioRxiv, p. 2020.10.13.337436, Jan. 2022, doi:10.1101/2020.10.13.337436.
[46] M.C. Ryan, P. Sherman, L.M. Rowland, S.A. Wijtenburg, A. Acheson, E. Fieremans, J. Veraart, D.S. Novikov, L.E. Hong, J. Sladky, P.D. Peralta, P. Kochunov, S.A. McGuire, Miniature pig model of human adolescent brain white matter development, J. Neurosci. Methods 296 (2018) 99–108, doi:10.1016/j.jneumeth.2017.12.017.
[47] H.A. Kinder, E.W. Baker, F.D. West, The pig as a preclinical traumatic brain injury model: current models, functional outcome measures, and translational detection strategies, Neural Regen. Res. 14 (3) (2019) 413–424 Mar, doi:10.4103/1673-5374.245334.
[48] Z. Zhou, A.G. Domel, X. Li, G. Grant, S. Kleiven, D. Camarillo, M. Zeineh, White matter tract-oriented deformation is dependent on real-time axonal fiber orientation, J. Neurotrauma 38 (12) (2021) 1730–1745 Jan, doi:10.1089/neu.2020.7412.
[49] A.J. Jasinska, C.A. Schmitt, S.K. Service, R.M. Cantor, K. Dewar, J.D. Jentsch, J.R. Kaplan, T.R. Turner, W.C. Warren, G.M. Weinstock, R.P. Woods, N.B. Freimer, Systems biology of the vervet monkey, ILAR J. 54 (2) (2013) 122–143 Jan, doi:10.1093/ilar/ilt049.
[50] H. Takemura, N. Palomero-Gallagher, M. Axer, D. Gräßel, M.J. Jorgensen, R. Woods, K. Zilles, Anatomy of nerve fiber bundles at micrometer-resolution in the vervet monkey visual system, eLife 9 (2020) e55444, doi:10.7554/eLife.55444.
[51] R. Gil-da-Costa, M.D. Hauser, Vervet monkeys and humans show brain asymmetries for processing conspecific vocalizations, but with opposite patterns of laterality, Proc. R. Soc. B Biol. Sci. 273 (1599) (2006) 2313–2318 Sep, doi:10.1098/rspb.2006.3580.
[52] M. Yan, W. Yu, Q. Lv, Q. Lv, T. Bo, X. Chen, Y. Liu, Y. Zhan, S. Yan, X. Shen, B. Yang, Q. Hu, J. Yu, Z. Qiu, Y. Feng, X.-Y. Zhang, H. Wang, F. Xu, Z. Wang, Mapping brain-wide excitatory projectome of primate prefrontal cortex at submicron resolution and comparison with diffusion tractography, eLife 11 (2022) e72534, doi:10.7554/eLife.72534.
[53] F. Xu, Y. Shen, L. Ding, C.-Y. Yang, H. Tan, H. Wang, Q. Zhu, R. Xu, F. Wu, Y. Xiao, C. Xu, Q. Li, P. Su, L.I. Zhang, H.W. Dong, R. Desimone, F. Xu, X. Hu, P.M. Lau, G.Q. Bi, High-throughput mapping of a whole rhesus monkey brain at micrometer resolution, Nat. Biotechnol. 39 (12) (2021) 1521–1528, doi:10.1038/s41587-021-00986-5.
[54] S. Simona, O.-P. Mario, B. Muhamed, P. Laurent, D. Maxime, T. Jean-Philippe, D. Alessandro, A new method for accurate *in vivo* mapping of human brain connections using microstructural and anatomical information, Sci. Adv. 6 (31) (2022) eaba8245 Jun, doi:10.1126/sciadv.aba8245.
[55] K.H. Maier-Hein, P.F. Neher, J.C. Houde, M.A. Côté, E. Garyfallidis, J. Zhong, M. Chamberland, F.C. Yeh, Y.C. Lin, Q. Ji, W.E. Reddick, J.O. Glass, D.Q. Chen, Y. Feng, C. Gao, Y. Wu, J. Ma, H. Renjie, Q. Li, C.F. Westin, S. Deslauriers-Gauthier, J.O.O. González, M. Paquette, S. St-Jean, G. Girard, F. Rheault, J. Sidhu, C.M.W. Tax, F. Guo, H.Y. Mesri, S. Dávid, M. Froeling, A.M. Heemskerk, A. Leemans, A. Boré, B. Pinsard, C. Bedetti, M. Desrosiers, S. Brambati, J. Doyon, A. Sarica, R. Vasta, A. Cerasa, A. Quattrone, J. Yeatman, A.R. Khan, W. Hodges, S. Alexander, D. Romascano, M. Barakovic, A. Auría, O. Esteban, A. Lemkaddem, J.-P. Thiran, H.E. Cetingul, B.L. Odry, B. Mailhe, M.S. Nadar, F. Pizzagalli, G. Prasad, J.E. Villalon-Reina, J. Galvis, P.M. Thompson, F.D.S. Requejo, P.L. Laguna, L.M. Lacerda, R. Barrett, F. Dell'Acqua, M. Catani, L. Petit, E. Caruyer, A. Daducci, T.B. Dyrby, T. Holland-Letz, C.C. Hilgetag, B. Stieltjes, M. Descoteaux, The challenge of mapping the human connectome based on diffusion tractography, Nat. Commun. 8 (1) (2017) 1349, doi:10.1038/s41467-017-01285-x.
[56] C. Maffei, G. Girard, K.G. Schilling, D.B. Aydogan, N. Adluru, A. Zhylka, Y. Wu, M. Mancini, A. Hamamci, A. Sarica, A. Teillac, S.H. Baete, D. Karimi, F.C. Yeh, M.E. Yildiz, A. Gholipour, Y. Bihan-Poudec, B. Hiba, A. Quattrone, A. Quattrone, T. Boshkovski, N. Stikov, P.T. Yap, A. de Luca, J. Pluim, A. Leemans, V. Prabhakaran, B.B. Bendlin, A.L. Alexander, B.A. Landman, E.J. Canales-Rodríguez, M. Barakovic, J. Rafael-Patino, T. Yu, G. Rensonnet, S. Schiavi, A. Daducci, M. Pizzolato, E. Fischi-Gomez, J.-P. Thiran, G. Dai, G. Grisot, N. Lazovski, S. Puch, M. Ramos, P. Rodrigues, V. Prčkovska, R. Jones, J. Lehman, S.N. Haber, A. Yendiki, Insights from the irontract challenge: optimal methods for mapping brain pathways from multi-shell diffusion MRI, Neuroimage 257 (2022) 119327, doi:10.1016/j.neuroimage.2022.119327.
[57] K.S. Anand, V. Dhikav, Hippocampus in health and disease: an overview, Ann. Indian Acad. Neurol. 15 (4) (2012) 239–246 Oct, doi:10.4103/0972-2327.104323.
[58] H. Duvernoy, F. Cattin, P.Y. Risold, in: H.M. Duvernoy, F. Cattin, P.-Y. Risold (Eds.), Anatomy BT - The Human Hippocampus: Functional Anatomy, Vascularization and Serial Sections with MRI, Springer Berlin Heidelberg, Berlin, Heidelberg, 2013, pp. 39–68, doi:10.1007/978-3-642-33603-4_4.
[59] H. Duvernoy, F. Cattin, P.Y. Risold, in: H.M. Duvernoy, F. Cattin, P.-Y. Risold (Eds.), Structure, Functions, and Connections BT - The Human Hippocampus: Functional Anatomy, Vascularization and Serial Sections with MRI, Springer Berlin Heidelberg, Berlin, Heidelberg, 2013, pp. 5–38, doi:10.1007/978-3-642-33603-4_3.
[60] H. Duvernoy, F. Cattin, P.Y. Risold, in: H.M. Duvernoy, F. Cattin, P.-Y. Risold (Eds.), Sectional Anatomy and Magnetic Resonance Imaging BT - The Human Hippocampus: Functional Anatomy, Vascularization and Serial Sections with MRI, Springer Berlin Heidelberg, Berlin, Heidelberg, 2013, pp. 127–213, doi:10.1007/978-3-642-33603-4_7.
[61] A.D. Ekstrom, A.J. Bazih, N.A. Suthana, R. Al-Hakim, K. Ogura, M. Zeineh, A.C. Burggren, S.Y. Bookheimer, Advances in high-resolution imaging and computational unfolding of the human hippocampus, Neuroimage 47 (1) (2009) 42–49, doi:10.1016/j.neuroimage.2009.03.017.
[62] M.B. Parekh, B.K. Rutt, R. Purcell, Y. Chen, M.M. Zeineh, Ultra-high resolution *in-vivo* 7.0T structural imaging of the human hippocampus reveals the endfolial pathway, Neuroimage 112 (2015) 1–6, doi:10.1016/j.neuroimage.2015.02.029.
[63] M.M. Zeineh, S. Holdsworth, S. Skare, S.W. Atlas, R. Bammer, Ultra-high resolution diffusion tensor imaging of the microscopic pathways of the medial temporal lobe, Neuroimage 62 (3) (2012) 2065–2082 Sep, doi:10.1016/j.neuroimage.2012.05.065.
[64] T.M. Shepherd, E. Özarslan, A.T. Yachnis, M.A. King, S.J. Blackband, Diffusion tensor microscopy indicates the cytoarchitectural basis for diffusion anisotropy in the human hippocampus, Am. J. Neuroradiol. 28 (5) (2007) 958–964.
[65] D.H. Adler, L.E.M. Wisse, R. Ittyerah, J.B. Pluta, S.-L. Ding, L. Xie, J. Wang, S. Kadivar, J.L. Robinson, T. Schuck, J.Q. Trojanowski, M. Grossman, J.A. Detre, M.A. Elliott, J.B. Toledo, W. Liu, S. Pickup, M.I. Miller, S.R. Das, D.A. Wolk, P.A. Yushkevich, Characterizing the human hippocampus in aging and Alzheimer's disease using a computational atlas derived from *ex vivo* MRI and histology, Proc. Natl. Acad. Sci. U. S. A. 115 (16) (2018) 4252–4257 Apr, doi:10.1073/pnas.1801093115.
[66] S. Ravikumar, L.E.M. Wisse, S. Lim, R. Ittyerah, L. Xie, M.L. Bedard, S.R. Das, E.B. Lee, M.D. Tisdall, K. Prabhakaran, J. Lane, J.A. Detre, G. Mizsei, J.Q. Trojanowski, J.L. Robinson, T. Schuck, M. Grossman, E. Artacho-Pérula, M.M.I. de Onzoño Martin, M. del Mar Arroyo Jiménez, M. Muñoz, F.J.M. Romero, M. del Pilar Marcos Rabal, S.C. Sánchez, J.C.D. González, C. de la Rosa Prieto, M.C. Parada, D.J. Irwin, D.A. Wolk, R. Insausti, P.A. Yushkevich, *Ex vivo* MRI atlas of the human medial temporal lobe: characterizing neurodegeneration due to tau pathology, Acta Neuropathol. Commun. 9 (1) (2021) 173, doi:10.1186/s40478-021-01275-7.
[67] K.-H. Tse, A. Cheng, F. Ma, K. Herrup, DNA damage-associated oligodendrocyte degeneration precedes amyloid pathology and contributes to Alzheimer's disease and dementia, Alzheimer's Dement. 14 (5) (2018) 664–679, doi:10.1016/j.jalz.2017.11.010.
[68] S. Safaiyan, N. Kannaiyan, N. Snaidero, S. Brioschi, K. Biber, S. Yona, A.L. Edinger, S. Jung, M.J. Rossner, M. Simons, Age-related myelin degradation burdens the clearance function of microglia during aging, Nat. Neurosci. 19 (8) (2016) 995–998, doi:10.1038/nn.4325.
[69] T. Iram, F. Kern, A. Kaur, S. Myneni, A.R. Morningstar, H. Shin, M.A. Garcia, L. Yerra, R. Palovics, A.C. Yang, O. Hahn, N. Lu, S.R. Shuken, M.S. Haney, B. Lehallier, M. Iyer, J. Luo, H. Zetterberg, A. Keller, J.B. Zuchero, T. Wyss-Coray, Young CSF restores oligodendrogenesis and memory in aged mice via Fgf17, Nature 605 (7910) (2022) 509–515, doi:10.1038/s41586-022-04722-0.
[70] H. Mathys, J. Davila-Velderrain, Z. Peng, F. Gao, S. Mohammadi, J.Z. Young, M. Menon, L. He, F. Abdurrob, X. Jiang, A.J. Martorell, R.M. Ransohoff, B.P. Hafler, D.A. Bennett, M. Kellis, L.-H. Tsai, Single-cell transcriptomic analysis of Alzheimer's disease, Nature 570 (7761) (2019) 332–337, doi:10.1038/s41586-019-1195-2.
[71] J.W. Blanchard, L.A. Akay, J. Davila-Velderrain, D. von Maydell, H. Mathys, S.M. Davidson, A. Effenberger, C.Y. Chen, K. Maner-Smith, I. Hajjar, E.A. Ortlund, M. Bula, E. Agbas, A. Ng, X. Jiang, M. Kahn, C. Blanco-Duque, N. Lavoie, L. Liu, R. Reyes, Y.-T. Lin, T. Ko, L. R'Bibo, W.T. Ralvenius, D.A. Bennett, H.P. Cam, M. Kellis, L.-H. Tsai, APOE4 impairs myelination via cholesterol dysregulation in oligodendrocytes, Nature (2022), doi:10.1038/s41586-022-05439-w.